Monthly Notices of the ROYAL ASTRONOMICAL SOCIETY

MNRAS **438,** 1922–1947 (2014) doi:10.1093/mnras/stt2213
Advance Access publication 2014 January 10

The Herschel Virgo Cluster Survey – XVI. A cluster inventory⋆

J. I. Davies,[1]† S. Bianchi,[2] M. Baes,[3] G. J. Bendo,[4] M. Clemens,[5] I. De Looze,[3] S. di Serego Alighieri,[2] J. Fritz,[3] C. Fuller,[1] C. Pappalardo,[6] T. M. Hughes,[3] S. Madden,[7] M. W. L. Smith,[1] J. Verstappen[3] and C. Vlahakis[8]

[1]*School of Physics and Astronomy, Cardiff University, The Parade, Cardiff CF24 3AA, UK*
[2]*INAF – Osservatorio Astrofisico di Arcetri, Largo Enrico Fermi 5, I-50125 Firenze, Italy*
[3]*Sterrenkundig Observatorium, Universiteit Gent, Krijgslaan 281 S9, B-9000 Gent, Belgium*
[4]*Jodrell Bank Centre for Astrophysics, School of Physics and Astronomy, University of Manchester, Oxford Road, Manchester M13 9PL, UK*
[5]*INAF – Osservatorio Astronomico di Padova, Vicolo dell' Osservatorio 5, I-35122 Padova, Italy*
[6]*CAAUL, Observatório Astronómico de Lisboa, Universidade de Lisboa, Tapada da Ajuda, P-1349-018 Lisboa, Portugal*
[7]*Laboratoire AIM, CEA/DSM – CNRS – Université Paris Diderot, Irfu/Service, F-91191 Paris, France*
[8]*Joint ALMA Observatory/European Southern Observatory, Alonso de Cordova 3107, Vitacura, Santiago, Chile*

Accepted 2013 November 7. Received 2013 November 5; in original form 2013 August 15

ABSTRACT

Herschel far-infrared (FIR) observations are used to construct Virgo cluster galaxy luminosity functions and to show that the cluster lacks the very bright and the numerous faint sources detected in field galaxy surveys. The FIR spectral energy distributions are fitted to obtain dust masses and temperatures and the dust mass function. The cluster is overdense in dust by about a factor of 100 compared to the field. The same emissivity (β)–temperature relation applies for different galaxies as that found for different regions of M31. We use optical and H I data to show that Virgo is overdense in stars and atomic gas by about a factor of 100 and 20, respectively. Metallicity values are used to measure the mass of metals in the gas phase. The mean metallicity is ∼0.7 solar, and ∼50 per cent of the metals are in the dust. For the cluster as a whole, the mass density of stars in galaxies is eight times that of the gas and the gas mass density is 130 times that of the metals. We use our data to consider the chemical evolution of the individual galaxies, inferring that the measured variations in the effective yield are due to galaxies having different ages, being affected to varying degrees by gas loss. Four galaxy scaling relations are considered: mass–metallicity, mass–velocity, mass–star formation rate and mass–radius – we suggest that initial galaxy mass is the prime driver of a galaxy's ultimate destiny. Finally, we use X-ray observations and galaxy dynamics to assess the dark and baryonic matter content compared to the cosmological model.

Key words: galaxies: clusters: individual: Virgo – galaxies: ISM.

1 INTRODUCTION

At 17–23 Mpc, the Virgo cluster is the nearest large grouping of galaxies to us. It has played a prominent role in astronomical research since the identification of an excess of nebulous objects in this area of sky was noted by both Messier and *Herschel*. It was first recognized as a group of extragalactic objects by Shapley & Ames (1926). The proximity of the Virgo cluster enables us to study both the general properties of galaxies and the way in which the cluster environment may have affected how galaxies evolve. The cluster contains a wide morphological mix of galaxies that subtend some of the largest angular sizes for extragalactic objects (the elliptical M87 subtends 7 arcmin, and the spiral M58 subtends a 6 arcmin diameter) and so allows us to study not only large numbers of galaxies, but also individual galaxies in detail.

Recent surveys of the Virgo cluster include X-ray (Bohringer et al. 1994), ultraviolet (Boselli et al. 2011), optical (VCC, Binggeli, Sandage & Tammann 1985; ACS, Cote et al. 2004; SDSS, Abazajian et al. 2009; VGVS, Mei et al. 2010), near-infrared (2MASS, Skrutskie et al. 2006; UKIDSS, Warren et al. 2007), far-infrared (*IRAS*, Neugebauer et al. 1984; *Herschel*, Davies et al. 2012) and 21 cm (ALFALFA, Giovanelli et al. 2005; VIVA, Chung et al. 2009; AGES, Taylor 2010). Prominent amongst these surveys is the optical survey of Binggeli et al. (1985), which listed about 2000 cluster members and has subsequently served as the primary input for many of the other surveys. Clearly, no other galaxy cluster

⋆*Herschel* is an ESA space observatory with science instruments provided by European-led Principal Investigator consortia and with important participation from NASA.
†E-mail: jid@astro.cf.ac.uk

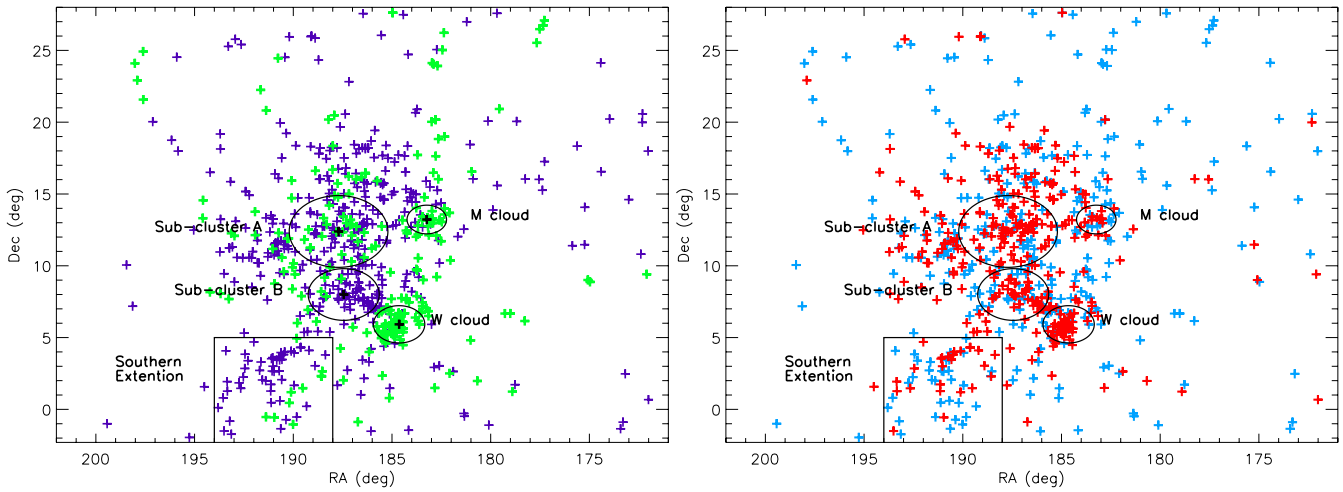

Figure 1. Data from a 30 × 30 square degree region centred on the Virgo cluster and extracted from the SDSS spectroscopic data. Left: galaxies with $400 < v_{\rm Helio} < 1600\,{\rm km\,s^{-1}}$ are shown in purple and those with $1600 < v_{\rm Helio} < 2659\,{\rm km\,s^{-1}}$ are shown in green. Right: galaxies with $(g - r) > 0.62$ are shown in red and those with $(g - r) < 0.62$ in blue. The circles and box indicate the various sub-structures discussed in the text.

has its galaxy population known to this level of detail, and for this reason we now intend to put these various data sources together to hopefully obtain a clearer picture of what constitutes the Virgo cluster.

Before starting on this inventory, we will set the scene by reviewing the cluster's structure and its environment. None of this discussion will be very new, but much of what was done in the past was drawn from various, numerous and very different data sources (Binggeli, Tammann & Sandage 1987; Binggeli, Popescu & Tammann 1993; Gavazzi et al. 1999) whereas we can now use the uniform Sloan Digital Sky Survey (SDSS) spectroscopic data (Strauss et al. 2002) to review the conclusions drawn by others.

The SDSS spectroscopic sample consists of spectra of all SDSS objects with a g-band magnitude of $\leq$17.7. From this extensive data set, we have selected all those objects that have been assigned a velocity of between 400 and 10 000 km s^{-1} within a 30 × 30 square degree region centred on M87 [RA(J2000) = 187.706, Dec.(J2000) = 12.391]. The minimum value of 400 km s^{-1} was chosen to avoid confusion with Galactic stars and the maximum value of 10 000 km s^{-1} is arbitrary, but we wanted to show the larger scale structure around Virgo.[1] We will adopt the distances to the various components of the cluster as given in Gavazzi et al. (1999). They use Tully–Fisher and Fundamental Plane scaling relations to obtain velocity-independent distances to many of the brighter cluster galaxies.

In Fig. 1, we show the distribution of cluster galaxies on the sky by limiting the velocity range to a maximum of ∼2700 km s^{-1}. As we will show below, this is the highest velocity of any of the galaxies in our *Herschel* sample and clearly, as shown in Fig. 2, this separates the cluster in velocity from other galaxies in other galactic structures. In Fig. 1 (left), we show the position of the galaxies separated into two velocity ranges; those with $400 < v_{\rm Helio} < 1600\,{\rm km\,s^{-1}}$ (463 galaxies) are shown in purple and those with $1600 < v_{\rm Helio} < 2659\,{\rm km\,s^{-1}}$ (227 galaxies) are shown in green. Fig. 3, discussed in more detail below, shows that the Virgo cluster galaxy velocity distribution is double peaked and that it roughly corresponds to the above two intervals. Following Binggeli et al. (1987), we identify five structures in Fig. 1 (left).

(i) Sub-cluster A – Galaxies around, but not exactly centred on M87, which has a velocity of about 1300 km s^{-1}. Binggeli et al. (1987) describe sub-cluster A as rich in early-type galaxies. Gavazzi et al. (1999) place sub-cluster A at 17 Mpc, a distance we will use in what follows.

(ii) Sub-cluster B – Galaxies around, but not exactly centred on M49, which has a velocity of about 1000 km s^{-1}. Binggeli et al. (1987) describe sub-cluster B as rich in late-type galaxies and say that it is falling into sub-cluster A from behind. Gavazzi et al. (1999) place sub-cluster B at 23 Mpc, again a distance we will use in what follows.

(iii) W cloud – Galaxies in this region seem to be isolated spatially and have a greater velocity (∼2200 km s^{-1}) than the sub-clusters. Binggeli et al. (1987) say that the distance to the W cloud is about twice that to the sub-clusters and that the W cloud is falling into the sub-clusters.

(iv) M cloud – Galaxies in this region again seem to be isolated spatially and have a greater velocity (∼2200 km s^{-1}) than the sub-clusters. Binggeli et al. (1987) say that the distance to the M cloud is again about twice that to the sub-clusters and that the M cloud is falling into the sub-clusters.

(v) Southern extension – there is a filamentary structure that extends to the south of the cluster. Galaxies in the southern extension are at about the same distance as the sub-clusters, and Binggeli et al. (1987) say that they also are falling into the sub-clusters.

Fig. 1 (right) is the same as on the left except that now the colour coding picks out intrinsically red and blue galaxies. We simply divided the sample of 690 galaxies in half at the median $(g - r)$ colour of 0.62. Crudely associating red with early and blue with late types we can see the morphology–density relation (Dressler 1980) with red galaxies more concentrated into the identified structures – the exception being the southern extension. Both of the clouds seem to contain their fair share of red galaxies indicating that whatever processes that give rise to the morphology–density relation operate on the scale of the clouds as well as on the scale of the sub-clusters.

[1] Note that velocities below 400 km s^{-1} are only excluded here so that the structure of Virgo can be seen in the figures and is not confused with other non-Virgo SDSS objects. There are of course Virgo galaxies with velocities less than 400 km s^{-1}, which will be included in all of the quantitative analysis described later.

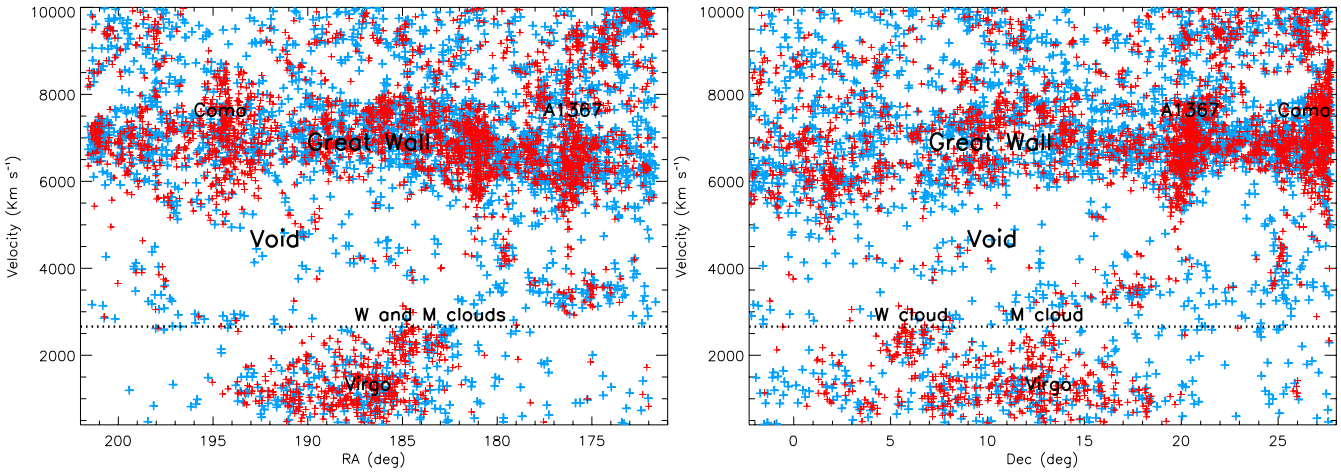

Figure 2. Left: right ascension against velocity for all SDSS spectroscopic data galaxies within 10 000 km s^{-1} over a 30 × 30 square degree region centred on the Virgo cluster. Galaxies with $(g - r) > 0.60$ are shown in red and those with $(g - r) < 0.60$ in blue. Right: the same as the figure on the left except this is now declination against velocity. The black dotted line indicates our velocity limit ($v_{\rm Helio} < 2659$ km s^{-1}) for the Virgo sample.

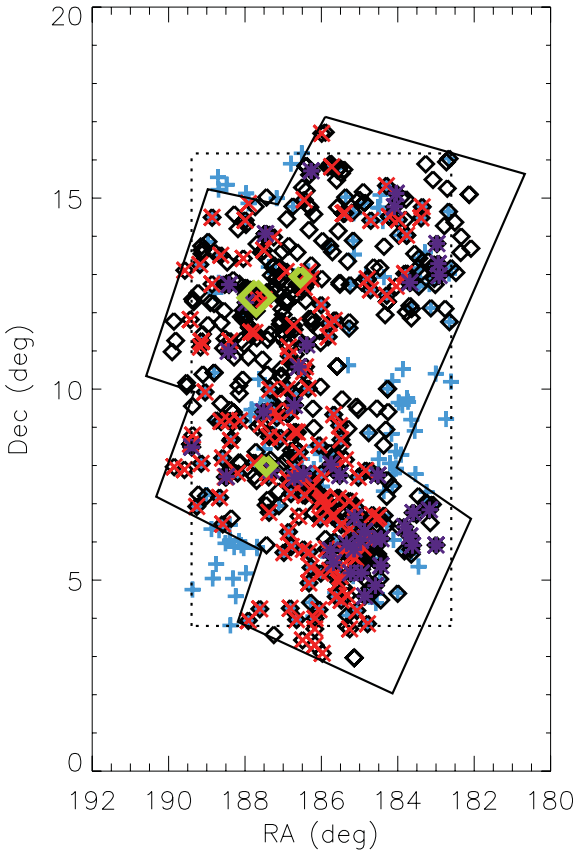

Figure 3. The positions on the sky of the galaxies used to measure the dynamical mass. Black diamonds denote the VVC+ sample, blue crosses the H I sample, red crosses the *Herschel* sample and purple diamonds the new SDSS optical detections. The large green diamond marks the position of M87, and the upper and lower smaller green diamonds mark the positions of M86 and M49, respectively. The solid black line shows the approximate outline of the region of sky observed by *Herschel*. The black dotted line shows the region extracted from the H I ALFALFA data.

To reveal the environment of the Virgo cluster, in Fig. 2 we show the full data set out to 10 000 km s^{-1} in position–velocity plots. Virgo (sub-clusters A and B) along with the W and M clouds are clearly distinguished in velocity because of the approximate 3000 km s^{-1} void that lies behind Virgo. The black dotted line is at $v \approx 2700$ km s^{-1} and clearly shows why we used this velocity to isolate Virgo cluster galaxies in Fig. 1. At about 6000 km s^{-1}, we find what has become known as the Great Wall, which is a huge filament of galaxies stretching across the sky. Contained within the Great Wall are two other well-known clusters Coma and A1367. In Fig. 2, we have again distinguished galaxies via their colour, splitting the sample of 5355 galaxies in half at $(g - r) = 0.60$. Again, the morphology–density relation is apparent on these much larger scales.

Having hopefully set the scene by briefly describing the structure of the cluster and the environment it resides within, we will now go on and consider the properties of the cluster and its constituent galaxies in much more detail. We will initially concentrate on the far-infrared properties of the galaxies as measured by the Herschel Observatory. We will then add to this new data from the SDSS, so that we can consider the stellar properties of the galaxies, and from the Arecibo Legacy Fast ALFA (ALFALFA) survey to consider the gas properties. In addition and where required, we will add information on X-ray gas, warm/hot gas, star formation rates (SFRs) and molecular gas to try and get as complete picture as possible of the cluster and its galactic population. We will then use these data to consider the chemical evolution of the galaxies and the cluster, its current SFR, galaxy scaling relations (mass, size, radius) and the total mass including the X-ray gas and dark matter. Finally, we will briefly compare the properties of the two sub-clusters A and B described above.

This paper is a continuation of a series of papers written by us, primarily using data taken from our *Herschel* guaranteed open time project the Herschel Virgo Cluster Survey (HeViCS). In the previous 13 papers, we have described: the survey and considered the properties of the bright galaxies in a single central 4 × 4 square degree field (Davies et al. 2010, Paper I), how the cluster environment truncates the dust discs of spiral galaxies (Cortese et al. 2010b, Paper II), the dust lifetime in early-type galaxies (Clemens et al. 2010, Paper III), the spiral galaxy dust surface density and

temperature distribution (Smith et al. 2010, Paper IV), the properties of metal-poor star-forming dwarf galaxies (Grossi et al. 2010, Paper V), the lack of thermal emission from the elliptical galaxy M87 (Baes et al. 2010, Paper VI), the far-infrared detection of dwarf elliptical galaxies (De Looze et al. 2010, Paper VII), the properties of the 78 far-infrared brightest cluster galaxies (Davies et al. 2012, Paper VIII), the dust-to-gas ratios and metallicity gradients in spiral galaxies (Magrini et al. 2012, Paper IX), the cold dust–molecular gas relationship (Corbelli et al. 2012, Paper X), the environmental effects on molecular gas and dust (Pappalardo et al. 2012, Paper XI), the far-infrared properties of 251 optically selected galaxies (Auld et al. 2013, Paper XII) and the dust properties of early-type galaxies (di Serego Alighieri et al. 2013, Paper XIII). A further five papers (Boselli et al. 2010, 2012; Cortese et al. 2012; Smith et al. 2012a,b) discuss HeViCS galaxies together with other galaxies observed as part of the Herschel Reference Survey (HRS).

2 DATA

We use as our starting point the *Herschel* data presented and described in Auld et al. (2013). This consists of observations of a total area of 84 square degrees made using *Herschel* in parallel scan map mode to obtain data in five bands (100, 160, 250, 350 and 500 μm). For a full discussion of this data and its reduction and calibration, we refer the reader to Davies et al. (2012) and Auld et al. (2013).

Using the fully reduced *Herschel* data, we then used the optically selected Virgo Cluster Catalogue (VCC; Binggeli et al. 1985) as the basis of a search for far-infrared emission from VCC members present in the *Herschel* data. The resulting galaxy sample is fully described in Auld et al. (2013), including a list of flux densities, dust masses and temperatures. Here, we give a brief summary. We used an automated routine to search for far-infrared emission at the position of the 750 VCC galaxies in our *Herschel* survey area. This resulted in the detection at 250 μm of 251 galaxies. Although it is not ideal to have an optical rather than a far-infrared selected sample, we have no other way of ensuring that we have a pure cluster sample rather than one contaminated by background sources. We will show below that there is no evidence for additional cluster far-infrared sources missed by our selection method.

The 251 galaxies listed by Auld et al. (2013) extend in distance (as given in the GOLDMINE data base; Gavazzi et al. 2003) from 17 to 32 Mpc with galaxy groupings at 17, 23 and 32 Mpc. This range of 15 Mpc in depth is large for a cluster and much larger than the linear size we survey on the plane of the sky (about 4 Mpc at a distance of 23 Mpc). For this reason, in this paper we restrict our analysis to galaxies with distances of 17 and 23 Mpc so that line-of-sight and plane of sky distances are comparable. These distances correspond to those of sub-cluster A containing M87 and sub-cluster B containing M49 (Gavazzi et al. 1999) – as described in the introduction. It excludes galaxies in the clouds and the southern extension. This leads to a surveyed volume of about 62.4 Mpc^3.[2] This distance scale is consistent with that recently measured by Mei et al. (2007) and with a Hubble constant of 73 $km\,s^{-1}\,Mpc^{-1}$, which we will use where required throughout this paper.

Restricting distances to between 17 and 23 Mpc leads to a sample of 208 galaxies. However, upon inspection of the data in GOLDMINE four of these were discovered to be listed as background galaxies (VCC12, VCC28, VCC40 and VCC262). A further galaxy VCC881(north) was removed because of its close proximity to VCC881(south) and hence possible confusion; this gives 203 galaxies. As described above, SDSS velocity data are now available for a flux-limited ($g \leq 17.7$) sample of galaxies over the Virgo cluster region. To see if we were missing any optical sources not included in the VCC (which was selected to almost equivalently $B \approx 18.0$), we searched the SDSS archive for galaxies over our survey area, which had a heliocentric velocity of 400–2600 $km\,s^{-1}$ – this led to 43 new optical detections. Four of these, new optical detections were subsequently found to have been detected in our *Herschel* data at 250 μm and these have been added to our list to make a total of 207 galaxies in our final sample – 147 at 17 and 60 at 23 Mpc. This gives a mean distance for our sample of 18.7 Mpc.[3]

In order to carry out our inventory of the cluster, we require, in addition to our *Herschel* data, information at other wavelengths. We have used (where available) *B*- and *H*-band magnitudes from the NASA Extragalactic Database (NED), 21 cm atomic hydrogen observations from the ALFALFA survey (Giovanelli et al. 2007), molecular hydrogen masses from Corbelli et al. (2012) and Young et al. (2011) and data from the compilation of galaxy metallicities and SFRs from Hughes et al. (2013). It is our intention to use correlations within these sparsely populated data sets to obtain the data we require for all 207 of our *Herschel* sample objects.

3 LUMINOSITY FUNCTIONS

The Auld et al. (2013) data are obtained from the positions of optically selected galaxies in the VCC. This is not ideal as we would prefer to select galaxies via their far-infrared flux density when constructing far-infrared luminosity functions. The problem of course is identifying which far-infrared sources belong to the cluster and which are in the background. To address this issue, we have carried out a faint galaxy number count analysis of the Virgo field and compared it to the faint galaxy number counts derived from the North Galactic Pole (NGP) field observed by the H-ATLAS consortium (Eales et al. 2010). We have done this at 250 μm because this is the wavelength at which the Auld et al. (2013) sample was selected, i.e. all the objects had to have a 250 μm detection. Our primary motivation for doing this is to compare the number counts from the general field (NGP) with that obtained by 'looking through' the Virgo cluster into the Universe beyond. In this way, we can assess the contribution made by the cluster to the total galaxy counts.

The NGP data are fully described in Valiante et al. (in preparation). To summarize, it consists of two orthogonal scans covering ∼180 square degrees of sky compared to the eight scans used for the Virgo data over ∼85 square degrees. The NGP data have been reduced using the same data reduction pipeline as the Virgo data, with the exception that the NGP data have been gridded on to a 5 arcsec pixel scale while the Virgo data use 6 arcsec pixels. We have used the source detection program SExtractor to extract faint sources from both the Virgo and NGP data, taking great care to apply identical methods to both fields. This is important because it quickly became apparent that very small changes in, for example, the threshold detection level can greatly alter the number of sources detected.

The Virgo field suffers from considerable cirrus contamination, which we substantially reduced by subtracting from the data a smoothed version of itself. The cirrus occurs on many spatial scales,

[2] The area of sky covered by the Herschel observations described here is about a factor of 1.3 larger than that used in Davies et al. (2012) because the area of sky covered by the full eight scan data set is larger.

[3] We assume that the new detections are at the mean distance of 18.7 Mpc.

but by subjectively considering the obvious features we decided on Gaussian smoothing with a full width at half-maximum of 11 arcmin to create the smoothed frame. As the *Herschel* data have a mean value of zero (by design), the subtraction conserves flux in the image. The subtraction 'flattens' the sky considerably, but does lead to some dark rings (negative values) around the brighter galaxy images because of their influence when deriving the local sky value. This should not be a problem as bright sources are least affected by sky brightness errors, and we are primarily interested in the possibility of there being faint (relatively small) galaxies in Virgo that we have missed via our optical source selection. We will show below that at bright magnitudes, the number counts are consistent with the Auld et al. (2013) data. The above does not rule out the possibility of there being rather large (∼10 arcmin or above) sized far-infrared sources in Virgo – these would be impossible to distinguish from the cirrus using our method.

Although the NGP field seems to be mostly devoid of Galactic cirrus, to be consistent we applied the same sky subtraction method to the NGP data. For a realistic comparison to be made between the two fields, we need to correctly account for the different noise characteristics of the two fields and see how this affects what SExtractor does. SExtractor measures the background noise over a specified area (mesh size) and uses this 'local' value to extract sources of a given size above some multiple of this noise. We chose the mesh size to be 100 arcmin^2, much larger than a typical galaxy. We then had to determine the fraction (f) of the background noise to set the detection threshold at, given the noise in the two data sets (NGP and Virgo). We experimented with multiple 100 arcmin^2 apertures to see how different the noise was both within and between the two data sets. The noise level was lower in the longer exposure Virgo data (but by only a factor of 0.9), but there was also a larger scatter in the values, presumably due to the residual Galactic cirrus (see below). We set the detection threshold at 1σ in the NGP field, which equated to a 1.6σ detection in the Virgo data with its larger pixels and lower noise per pixel. We set the minimum detection size to that of the 250 μm beam area of 423 arcsec^2.

The derived number counts for both the NGP and Virgo fields are shown in Fig. 4. The solid black line shows the NGP number counts. The counts are consistent with other counts and detection methods used in previous H-ATLAS data (Clements et al. 2010). The green dashed line has a slope of 1.5, which is what is expected for a non-evolving Euclidean universe. The line has been drawn to illustrate the sharp rise in the counts above a 'flat non-evolving' model at a flux density of about 0.2 Jy, as previously shown by Clements et al. (2010). The black dotted line indicates the minimum possible flux density for a source of the size of the beam with all pixels at 1σ above the background (0.013 Jy). The solid red line shows the counts in the Virgo field. The excess of bright cluster sources is clearly seen departing from the background at about 1 Jy. The blue line is for the original 251 galaxies from the Auld et al. (2013) sample and is consistent with the bright galaxy data (>1 Jy) obtained using SExtractor (solid red line).

The important question is whether there is a faint galaxy excess in the Virgo field that might be associated with a far-infrared population not detected using our optical source list. Looking at Fig. 4, we can see that below about 1 Jy the black line traces the red line very well and there is no evidence for an excess population over and above that detected by our optical selection. To be sure of this conclusion, we have assessed the effect of changing our detection threshold. As stated above, the variation in detection threshold (calculated within the mesh size) is quite consistent across the NGP field, but does vary across the Virgo field. We have calculated the

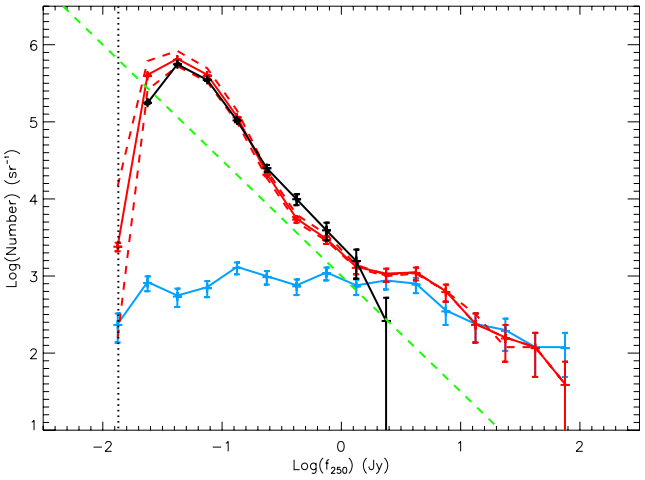

Figure 4. The Virgo field 250 μm faint galaxy number counts (solid red line) compared to the faint galaxy number counts in the general field as measured in the H-ATLAS NGP data (solid black line). The red dashed lines indicate lower and upper level expectations for the Virgo counts given the variations in sky noise in the Virgo field, which suffers from larger Galactic cirrus contamination. The blue line shows the number counts using the 251 galaxies from the Auld et al. (2013) data. The green dashed line has a slope of 1.5 and indicates the expected counts for a non-evolving Euclidean universe. The black dotted line indicates the minimum flux density detectable given the minimum detection area and 1σ noise level in the NGP data.

standard deviation of the 1σ fluctuations over fifty 100 arcmin^2 areas in the Virgo field to see how this influences the Virgo counts. We have used this standard deviation to see how changes in the threshold across the field influence the counts. The effect of these threshold variations is shown by the red dashed lines in Fig. 4. Clearly, the effect of these changes in the threshold value does not alter our conclusion that the optical selection is picking up most, if not all, of the far-infrared sources in the cluster.

Given the above discussion, we conclude that there is no good evidence for an additional population of faint far-infrared sources that is not associated with the previously identified optical sources. Based on this, below we proceed to construct luminosity functions.

Using the Auld et al. (2013) data, we can greatly extend and update the far-infrared luminosity functions presented in Davies et al. (2012). From the sample definition in Auld et al. (2013), all galaxies have a detection at 250 μm, but not necessarily at the other wavelengths. To make the data sets complete for all 207 galaxies across all wavelengths, we have used the mean observed flux density ratios (with 250 μm) to predict the missing flux density values. Of the 207 galaxies, 46, 37, 22 and 47 galaxies have had their data predicted by this means using ratios (F_λ/F_{250}) of 1.11, 1.34, 0.52 and 0.25 at 100, 160, 350 and 500 μm, respectively.

In Fig. 5, we show the derived luminosity functions with the best-fitting Schechter functions. The diamond symbols show the data before the adjustment for missing values was made, and the crosses after correcting for missing values. The adjustment predominantly affects the faint end of each luminosity function. The Schechter parameters of each fit are given in Table 1 using where necessary the cluster volume of 62.4 Mpc^{-1}. As we will see, when comparing to other far-infrared luminosity functions, the Virgo luminosity functions are characterized by a flat faint-end slope ($\alpha \approx -1.0$).

To illustrate the disparity between the cluster and field luminosity functions, we also show in Table 1 the Schechter fitting parameters for luminosity functions derived by others – see also Fig. 6. The *IRAS* 'field' 100 μm data come from the compilation of 629 galaxies

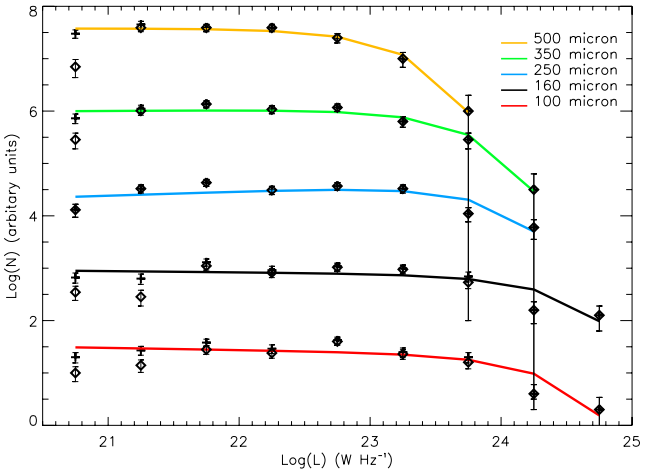

Figure 5. Virgo cluster galaxy luminosity functions for the five *Herschel* far-infrared bands. The solid lines denote the best-fitting Schechter functions to the complete adjusted data. The points marked by a diamond are for the unadjusted data. Data have been arbitrarily offset from each other.

in the bright galaxy sample of Sanders et al. (2003). We have simply used the galaxy distances to measure the relevant detection volumes. The *Herschel* data come from the H-ATLAS survey (Eales, private communication) using data from the three SPIRE bands at 250, 350 and 500 μm. The *Planck* data are taken directly from Negrello et al. (2013).[4]

The most disparate wavelength between the cluster and the field is 100 μm, where the *IRAS* luminosity function of nearby bright galaxies is considerably steeper at the faint end than that in the cluster. Sanders et al. (2003) (using the 'bolometric' infrared luminosity rather than the 100 μm flux density used here) actually fit the luminosity function with two power laws, one of slope $\alpha = -0.6$ and at the faint end with $\alpha = -2.2$,[5] compared to our single Schechter function fitted with $\alpha = -2.1$. With a slope of $\alpha = -1.0$, our cluster luminosity function either lacks faint dusty galaxies and/or the star formation required to heat the dust. We will return to the issue of dust mass and dust heating in Section 4. Another noticeable difference between the cluster and the field is the lack of very luminous infrared sources in the cluster – the derived L^*_{100} for the field is about a factor of 20 higher than that in the cluster. Given that the density of L^*_{100} galaxies in the field is only about 10^{-5} Mpc^{-3} even with a cluster overdensity of about 100, we would still only expect 1 in every 1000 Mpc^{-3} or about a 10 per cent chance of finding one in our cluster volume. Without studying more clusters, we cannot say whether we are unlucky or that clusters do not contain bright far-infrared sources, though the lack of bright sources in clusters has previously been noted by Bicay & Giovanelli (1987). With a faint-end slope of $\alpha > -2.0$, the *IRAS* luminosity function is unbound and we cannot calculate a luminosity density [$\rho_{\rm FIR} = \phi L^* \Gamma(2.0 + \alpha)$].

Comparing our Virgo longer wavelength luminosity functions with others, we find that a steeper faint-end slope and a larger value of L^* are a common feature of the field. Recently, Eales et al. (private communication) have derived the 250, 350 and 500 μm luminosity functions using H-ATLAS data for galaxies with $z \leq 0.1$ ($D \leq 411$ Mpc). Negrello et al. (2013) have done a similar thing using *Planck* 350 and 550 μm data for galaxies with $D \leq 100$ Mpc, see Table 1 and Fig. 6. When comparing the two, the *Planck* data give a steeper faint-end slope, about the same L^* and a luminosity density a factor of about 2 higher than the *Herschel* data. Generally, the cluster has a far-infrared luminosity density about two orders of magnitude higher than that of the field. The far-infrared luminosity density values given in Table 1 are about a factor of 2 higher than those given in table 2 of Davies et al. (2012), which were derived by summing the contributions of the bright galaxies rather than fitting and then integrating a Schechter luminosity function.

The issue of the differences between the local 'field' luminosity functions of *Herschel* H-ATLAS and *Planck* does not concern us here, but the differences between the cluster and the field do. It is clear that at all far-infrared wavelengths there is a lack of fainter sources in the cluster compared to what is generally found in the local field. Explanations could be that there is either a relative lack of emitting dust, it is cold or if far-infrared emission is closely connected to star formation (see below) then there is a lack of star formation in low-luminosity cluster systems.

4 DUST MASS, TEMPERATURE AND EMISSIVITY INDEX

We have used the 100–500 μm data to fit modified blackbody curves to the far-infrared spectral energy distributions (SEDs) of the 207 Virgo galaxies detected by *Herschel*. We have done this in two ways. First, we use a power-law dust emissivity $\kappa_\lambda = \kappa_0(\lambda_0/\lambda)^\beta$ with $\kappa_0 = 0.192$ m^2 kg^{-1} at $\lambda_0 = 350$ μm and a fixed $\beta(=2)$. Secondly, the same as above but now with a variable β. The fit is obtained using a standard χ^2 minimization technique as is fully described in Smith et al. (2012b). As discussed in Davies et al. (2012) (see their fig. 6), many galaxy far-infrared SEDs fit modified blackbodies with $\beta = 2$ very well, but here we wish to see if we can learn a little more by letting β vary as well.

Given the *Herschel* calibration (Davies et al. 2012) and the fitting procedure (Smith et al. 2012a), we estimate dust mass errors of the order of 25 per cent and temperature errors of the order of 10 per cent for both methods of fitting. In Fig. 7, we compare dust masses derived using both methods. In general, fixing $\beta = 2$ leads to higher dust masses than allowing β to be a variable parameter – median dust mass for $\beta = 2$ is 3.1×10^6 M$_\odot$ while for a free β it is about 22 per cent smaller (see also Bendo et al. 2003; Galametz et al. 2012).[6] This median dust mass compares with a recent determination of a median dust mass of 5.0×10^6 M$_\odot$ for galaxies in the local volume ($d < 100$ Mpc) as derived by Clemens et al. (2013) using the Negrello et al. (2013) sample described earlier (same β, but adjusted by a factor of 1.2 to account for the different emissivity normalizations used). There is no significant difference between the average dust mass of Virgo cluster galaxies and those found in the local field.

[4] We have multiplied the *Planck* 550 μm flux densities by 1.35 to make them approximately equivalent to the *Herschel* 500 μm data, see Baes et al. (2014).

[5] This *IRAS* bolometric luminosity function is consistent with recent measurements made by Magnelli et al. (2013) of the 8–1000 μm luminosity function based on PACS 70, 100 and 160 μm data.

[6] Note that Bianchi (2013) has shown that these differences in dust mass, calculated for different values of β, are actually spurious because they are based on a $\beta = 2.0$ normalization (κ_0). So the differences in mass we find are actually a reflection of our lack of knowledge of the dust emissivity function. Throughout the rest of this paper, we will use the dust masses calculated using $\beta = 2.0$.

Table 1. Schechter function fitting parameters for our *Herschel* data of the Virgo cluster. For comparisons, we also show the fitted parameters for field galaxies using the *IRAS* 100 μm data of Sanders et al. (2003), the *Herschel* 250, 350 and 500 μm data of Eales et al. (in preparation) and the *Planck* 350 and 550 μm data of Negrello et al. (2013). Note the *Planck* 550 μm data have been adjusted to correspond to the *Herschel* 500 μm band – the see text.

Band (μm)	Instrument	Region	α	L^* (10^{24} W Hz^{-1})	ϕ (Mpc^{-3} dex^{-1})	$\rho_{\rm FIR}$ (10^{23} W Hz^{-1} Mpc^{-3})
100	*Herschel*	Virgo	-1.0 ± 0.1	2.1 ± 0.6	0.3 ± 0.1	3.3
160	*Herschel*	Virgo	-1.0 ± 0.1	2.8 ± 1.0	0.3 ± 0.1	4.5
250	*Herschel*	Virgo	-0.9 ± 0.1	0.8 ± 0.2	0.6 ± 0.1	2.2
350	*Herschel*	Virgo	-1.0 ± 0.1	0.5 ± 0.1	0.5 ± 0.1	1.2
500	*Herschel*	Virgo	-1.0 ± 0.1	0.2 ± 0.01	0.5 ± 0.1	0.4
100	*IRAS*	Field	-2.1 ± 0.1	46 ± 15	$0.000\,012 \pm 0.000\,007$	–
250	*Herschel*	Field	-1.19 ± 0.04	1.6 ± 0.1	0.0017 ± 0.0002	0.03
350	*Herschel*	Field	-1.22 ± 0.05	0.7 ± 0.1	0.0014 ± 0.0002	0.01
500	*Herschel*	Field	-1.58 ± 0.12	0.4 ± 0.1	0.0067 ± 0.0003	0.01
350	*Planck*	Field	-1.65 ± 0.08	0.9 ± 0.1	0.0013 ± 0.0003	0.03
550	*Planck*	Field	-1.78 ± 0.1	0.4 ± 0.1	0.0010 ± 0.0003	0.02

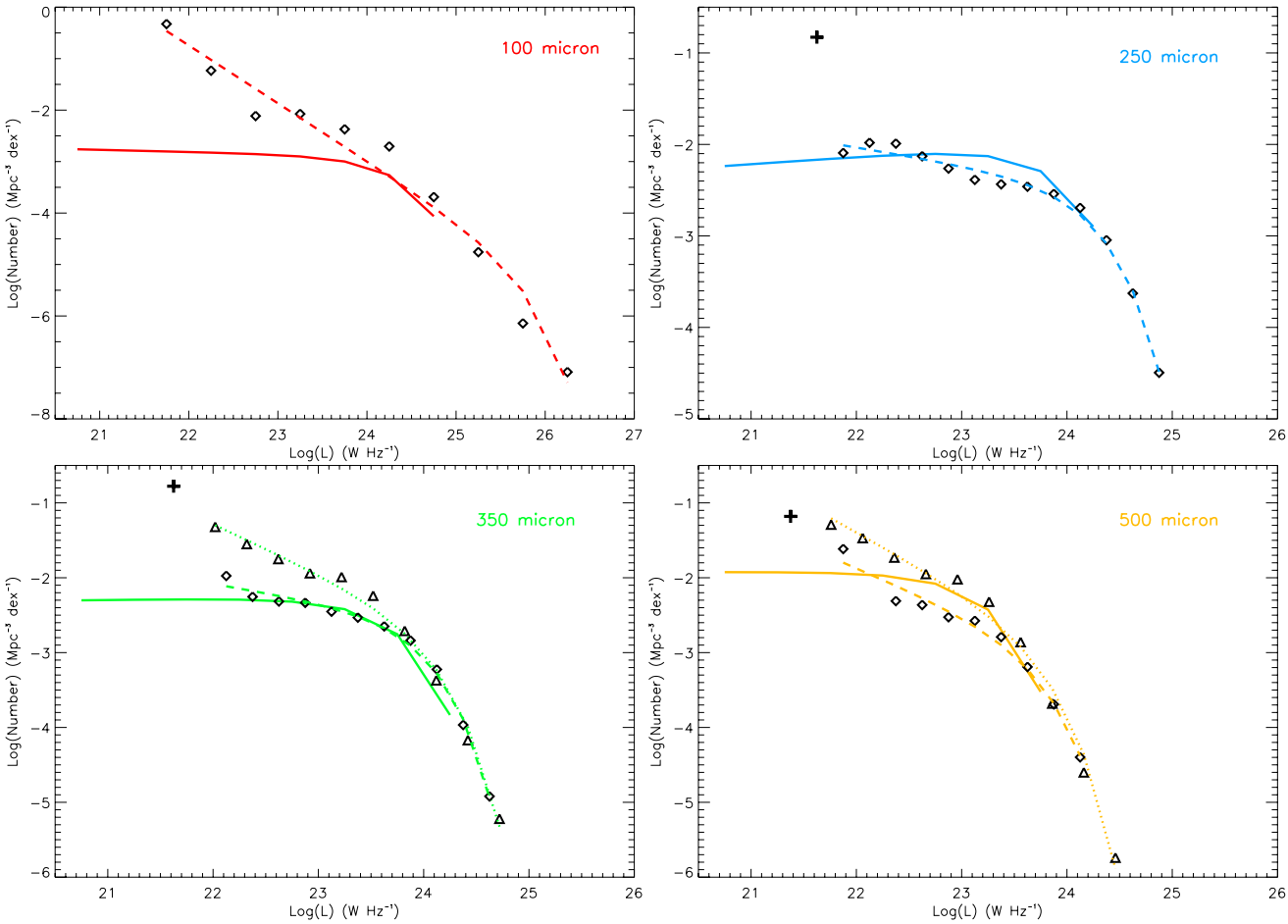

Figure 6. A comparison of luminosity functions at different wavelengths and over different environments. 100 μm – data points are from the *IRAS* survey of Sanders et al. (2003) and the dashed line shows the Schechter function fit. The solid line shows the Virgo luminosity function from Fig. 5 normalized at L^*. 250 μm – data points come from Eales et al. (in preparation) and the dashed line shows the Schechter function fit ignoring the lowest luminosity point marked by a cross. The solid line denotes the Virgo luminosity function from Fig. 5 normalized at L^*. 350 μm – the diamond data points come from Eales et al. (in preparation) and the dashed line shows the Schechter function fit ignoring the lowest luminosity point marked by a cross. The triangular data points come from Negrello et al. (2013) and the dotted line denotes the Schechter function fit. The solid line shows the Virgo luminosity function from Fig. 5 normalized at L^*. 500 μm – the diamond data points come from Eales et al. (in preparation) and the dashed line shows the Schechter function fit ignoring the lowest luminosity point marked by a cross. The triangular data points come from Negrello et al. (2013) and the dotted line shows the Schechter function fit. The solid line shows the Virgo luminosity function from Fig. 5 normalized at L^*.

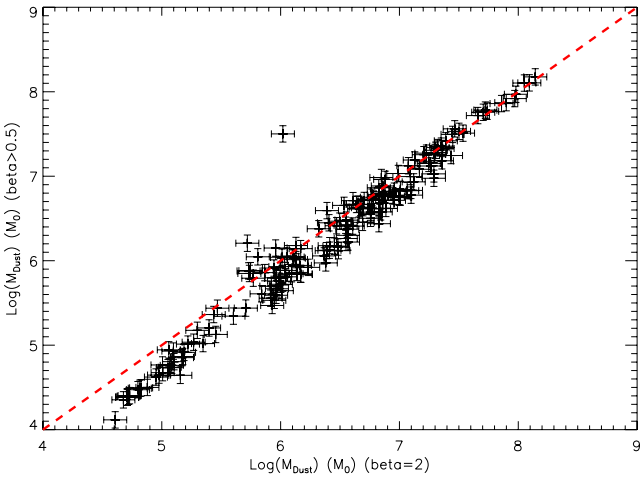

Figure 7. The relationship between dust mass derived using a fixed value of dust emissivity index $\beta = 2$ and a variable value. The red dashed line shows the one-to-one relationship.

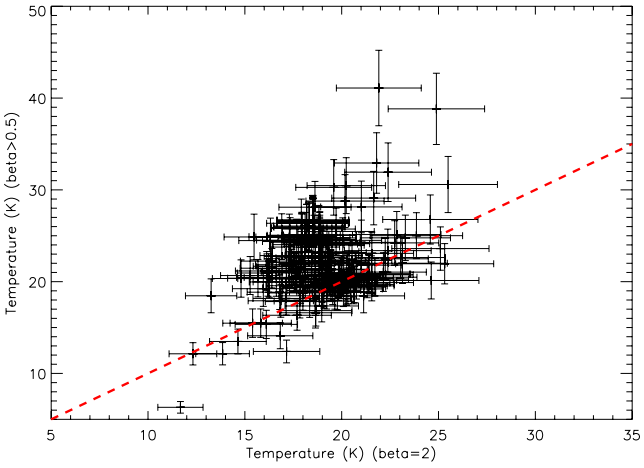

Figure 8. The relationship between dust temperature derived using a fixed value of dust emissivity index $\beta = 2$ and a variable value. The red dashed line shows the one-to-one relationship.

Similar differences occur in the derived temperatures. A fixed β leads to a median temperature of 18.9 K with a free β temperature about 16 per cent higher (Fig. 8). This again compares with a median temperature for galaxies in the Clemens et al. (2013) sample of 17.7 K. These temperatures for individual galaxies also compare very well with those recently measured for individually resolved regions in other nearby galaxies (Bendo et al. 2012; Galametz et al. 2012; Smith et al. 2012b; Draine et al. 2013) and with the Milky Way equilibrium dust temperature of 17.5 K (Lagache et al. 1998).

One might hope that by deriving individual values for β he could learn more about how the properties of the dust might vary between galaxies because the dust emissivity index β is related to the physical properties of the dust grains, i.e. composition, size and temperature (Dunne et al. 2011; Skibba et al. 2011; Smith et al. 2012a). Low values of β are thought to be associated with freshly formed dust in circumstellar discs or stellar winds. $\beta \approx 1$ is thought to be associated with small grains while $\beta \approx 2$ with larger grains formed through grain coagulation or the growth of ice mantels (Aannestad 1975; Seki & Yamamota 1980; Lis et al. 1998; Stepnik et al. 2003). Values for β in our Galaxy and in M31 range typically from about 0.5 to 3.0 (Planck Collaboration 2011; Smith et al. 2012a). A similar range for

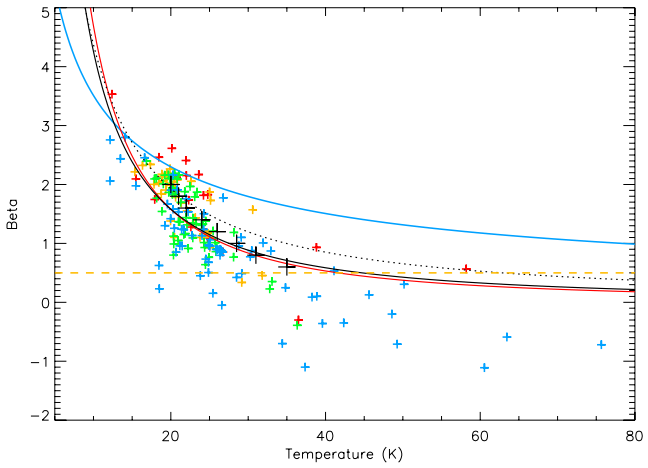

Figure 9. The relationship between dust temperature and dust emissivity index for 193 Virgo cluster galaxies. Galaxies are distinguished by their morphological type – earlier than Sa (red), Sa/Sb (yellow), Sc (green) and later than Sc (dwarfs and blue compact dwarfs) (blue). The solid black line shows the best-fitting line to the model described in the text using 146 galaxies later than S0. The black dotted line denotes the best-fitting line to the model described in the text using 19 galaxies earlier than Sa (red points). The blue line shows the relationship derived for regions within $R = 3.1$ kpc and the red line for $R > 3.1$ kpc as measured for M31 by Smith et al. (2012b). The dashed yellow line indicates a value of $\beta = 0.5$. The large black crosses indicate the $\beta - T$ relation derived for local field galaxies by Clemens et al. (2013).

β has also been measured by Clemens et al. (2013) using the *Planck* local volume sample of 234 galaxies (median value of $\beta = 1.83$).

193 galaxies in our sample were fitted with the variable β model (for 14 galaxies the fit did not converge). For those galaxies with $\beta > 0.5$ (see below), the median value of β is 1.43 (error on the mean value is 0.06), a little lower than that found by Clemens et al. (2013). In Fig. 9, we plot the derived values of β against the derived temperature. Clearly, values of β fall to lower values ($\beta < 0.5$) than have been observed in our Galaxy and M31. After inspecting the spectra we suggest three reasons why this is so. First, we have in our sample galaxies that not only have thermal emission from dust at these wavelengths, but also to varying degrees contaminating synchrotron emission from an active nucleus. For example, the emission from the giant central elliptical galaxy M87 is dominated by synchrotron (Baes et al. 2010; Davies et al. 2012) and when fitted to a modified blackbody gives a spurious $\beta = -2.7$. Secondly, some objects seem to have 'excess' 100 μm emission, which we interpret as being due to a prominent hot dust component associated with star formation (Bendo et al. 2012). In this case, a single dust component is again an inadequate interpretation of the data. Thirdly, for some galaxies there is emission at longer wavelengths over and above normal expectations (as observed for example in the Large Magellanic Cloud; Gordon et al. 2010). This additional long-wavelength emission can be particularly pronounced in dwarf star-forming galaxies (Dale et al. 2012; Remy-Ruyer et al. 2013) and can lead to unrealistically low values of β. The latter case leads to what we might describe as 'reasonable values' of the temperature while the first two produce very high unrealistic temperatures. When fitting to a single temperature, modified blackbody values of $\beta < 1$ are generally unphysical (Li 2004). The above highlights the problem of relating β to the changing physical properties of the dust.

Given the observation by Smith et al. (2012a), that what we expect to be pure thermal emission from the disc of M31 has $\beta > 0.5$,

we will use this as a discriminating value for those galaxies that have far-infrared SEDs that are well fitted by a single modified blackbody – 165 of the 207 galaxies in the sample have $\beta > 0.5$. In Fig. 9, we show the relationship between the derived temperature and the emissivity index β (those above the yellow dashed line have $\beta > 0.5$). There is clearly a relationship between these two parameters.

The origin of this relation has previously been debated and extensively discussed in Smith et al. (2012a). In summary, it has been proposed that the relationship may not be physical but rather the result of the fitting process (Shetty et al. 2009) and/or of fitting a one-component modified blackbody to a range of temperatures (Shetty et al. 2009). This point has also been made by Desert et al. (2008) who clearly show how errors in their derived values of β and T can lead to a false correlation, but they also show that the range of their data is greater than that expected solely due to these errors. Hence, they suggest that there might be something to be learned about the physical properties of the dust from the relation. As a further indicator that the $\beta-T$ relation has some physical basis, Smith et al. (2012a) show that for M31 the relationship is different for regions within and outside a radius of 3.1 kpc, which is the distance from the nucleus of the molecular (dusty) ring. They consider this to be an indicator of different dust within these two regions. If the relationship is physical, then it contains important information about the properties of the grains and provides motivation for a grain model that reproduces the relation (Meny et al. 2007; Coupeaud et al. 2011).

We can compare the $\beta-T$ relation we find with that obtained by others. Included in Fig. 9 are the two best-fitting lines of Smith et al. (2012a) to the inner (blue) and outer (red) dust of M31 (their equation 6). Using the same fitting parametrization ($\beta = A(\frac{T}{20\,\mathrm{K}})^{\alpha}$), we find best-fitting values of $A = 1.58$ and $\alpha = -1.44$ for galaxies with $\beta > 0.5$ and types later than S0 (our types 2, 3 and 4, see below). This fits the $R > 3.1$ kpc data for M31 almost exactly (see Fig. 9). If the $\beta-T$ relation is physical, then the range of conditions found in the disc of M31 is also to be found globally in the different late-type galaxies that make up the Virgo sample. With regard to our Galaxy, Paradis, Bernard & Meny (2009) have fitted SEDs to data from the balloon-borne instrument Archeops. They find a similar though flatter $\beta-T$ relation to ours (their value of T for $\beta = 2$ is 14.1 while ours is 17 K), though this is for individual sources rather than the diffuse emission across the sky, which may be more closely related to the global measurements of galaxies that we have. Clemens et al. (2013) also find a similar $\beta-T$ relation for their local *Planck* sample and we have plotted this as the large black crosses in Fig. 9 – it is in good agreement with what we find given the temperature errors on their points and our line of typically 2–5 K.

To look for different dust in different types of galaxies in Fig. 9, we have also identified morphological types (obtained from GOLDMINE) – 21 galaxies earlier than Sa (red), 41 galaxies Sa/Sb (yellow), 54 galaxies Sc (green) and 77 galaxies later than Sc (Sd, dwarfs and blue compact dwarfs) (blue). Roughly Sa/Sb/Sc galaxies occupy the same region of the $\beta-T$ plane as the individual resolved regions of M31 (Smith et al. 2012a). Early-type galaxies tend to have higher values of β for a given temperature than is typical for the later types (Smith et al. 2012b). There is a 'hint' in the data that maybe early-type galaxies follow the inner region relationship for M31 (blue line, Fig. 9) rather than the spiral galaxy relationship. The black dotted line represents a fit to the early-type galaxy data and although it is displaced towards the blue line it is by no means a close fit to it. The greatest scatter in Fig. 9 is produced by those galaxies listed as Sd/dwarf/BCD (blue compact dwarf). As

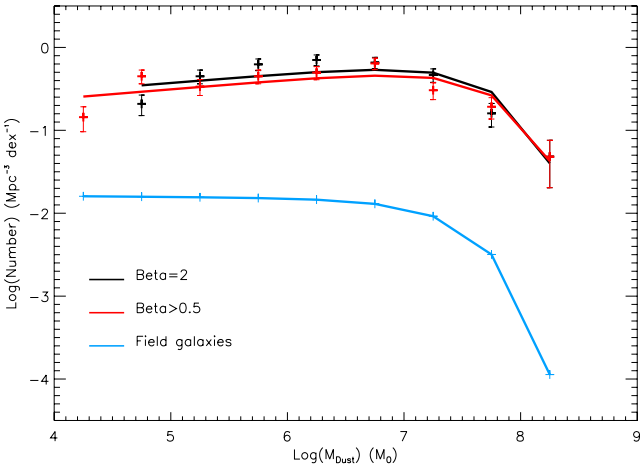

Figure 10. The dust mass function. The black line is for all 207 galaxies which have either measured or predicted flux densities in all five *Herschel* bands and have then been fitted with a $\beta = 2$ model. The red line is for the 165 galaxies that have been fitted to a variable β model and have values of $\beta > 0.5$. The blue line shows the field galaxy dust mass function taken from Dunne et al. (2011).

Table 2. Schechter function fitting parameters to the Virgo cluster dust mass function. For comparisons, we also give the values for the field taken from Dunne et al. (2011).

Sample	α	M^*_{Dust} (10^7 M$_\odot$)	ϕ (Mpc^{-3} dex^{-1})	ρ_{Dust} (10^7 M$_\odot$ Mpc^{-3})
$\beta = 2$	-0.9 ± 0.1	5.7 ± 1.3	0.7 ± 0.1	1.8
$\beta > 0.5$	-0.9 ± 0.1	6.1 ± 1.3	0.6 ± 0.1	1.7
Field	-1.0	3.6	0.006	0.02

stated above, these late-type galaxies with low values of $\beta < 0.5$ are inadequately fitted by a single modified blackbody because they appear to have a quite prominent warm dust component and so necessitate a more complex SED modelling approach – something we will explore in a later paper.

Having dust masses for our galaxies, we can construct the dust mass function in a similar way to the luminosity functions described earlier (Fig. 10). We have done this separately for the complete sample of 207 galaxies using both the observed and predicted *Herschel* flux densities and for the sample of 165 galaxies with variable $\beta > 0.5$. The fitted mass function parameters are given in Table 2 – they are very similar for both samples with the total dust mass density in the smaller $\beta > 0.5$ sample being only about 6 per cent less than that in the full sample of 207 galaxies. Note that the dust mass function value of M^*_{Dust} is very close to the value recently measured for M31 (5.4×10^7 M$_\odot$) by Draine et al. (2013). By using this larger sample and also by fitting a mass function, rather than just summing the contribution of the bright galaxies, we have increased our estimate of the cluster dust mass density, given in Davies et al. (2012), by about a factor of 7 (Table 2).

We have also compared our dust mass function parameters with those obtained for the general field by Dunne et al. (2011, table 2). We have used the Dunne et al. (2011) dust mass function because it is derived in a similar way to ours using *Herschel* data over wavelengths of less than 500 μm. However, we note that the recent dust mass function derived by Clemens et al. (2013) shows a steeper low-mass slope of $\alpha = -1.3$, although it compares reasonably well with Dunne et al. at the high-mass end ($M_{\mathrm{Dust}} > 10^8$ M$_\odot$).

The Clemens et al. (2013) dust mass function uses *Planck* data at wavelengths greater than 500 μm and so this may indicate that even the *Herschel* data miss cold dust, particularly in lower dust mass galaxies. We are in the process of compiling, where possible, *Planck* data on the galaxies in this sample (Baes et al. 2014).

Continuing our comparison with the Dunne et al. (2011) dust mass function, the derived dust mass density is about a factor of 100 higher in the cluster than it is in the field. All three mass functions shown in Fig. 10 are essentially flat at the low-mass end with no evidence for them being different in this respect between the cluster and the field. This is in contrast to the luminosity functions which were all steeper in the field than in the cluster. This can only come about if we have generally hotter dust in the lower luminosity field galaxies. We might have expected that if dust stripping processes are important in the cluster environment that the relative numbers of low and high dust mass galaxies may have changed between the cluster and the field, i.e. lower mass galaxies more readily losing their dust, but this does not appear to be so.

5 STELLAR MASS

Where possible we have followed the prescription of Bell et al. (2003) to derive stellar masses using

$$\log(M_{\rm Star}) = -0.339 + 0.266(g-r) + \log\left(\frac{L_{\rm H}}{L_{\odot}}\right).$$

Optical and near-infrared data were obtained directly from the NED for 130 of the 207 galaxies. Where there were insufficient data, we have simply used the linear relation between the mass derived using the B-band magnitude ($M^B_{\odot} = 5.48$) only and that calculated using the Bell et al. (2003) formula to estimate stellar masses (blue dashed line in Fig. 11). The stellar mass function derived in this way for the 207 galaxies in our *Herschel* sample is shown as the black line in Fig. 12. The mass function fitting parameters are given in Table 3. The low-mass slope (α) for both the dust and stellar mass functions is approximately the same again indicating that there is no preferential removal of dust from low-mass systems in the cluster environment. Using the derived densities, the stars-to-dust mass ratio for these galaxies is ∼1000, as might have been expected from observations of a 'typical' galaxy like the Milky Way.

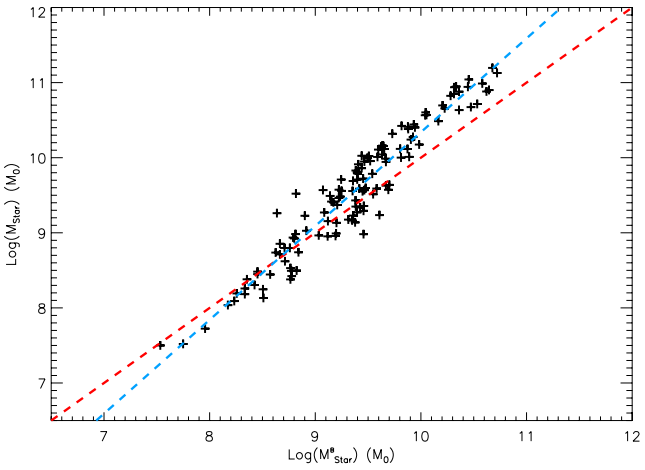

Figure 11. The relationship between the stellar masses derived from just B-band data (x-axis) and that obtained using the method described in the text (y-axis). The dashed red line shows the one-to-one relationship and the dashed blue line the best-fitting line.

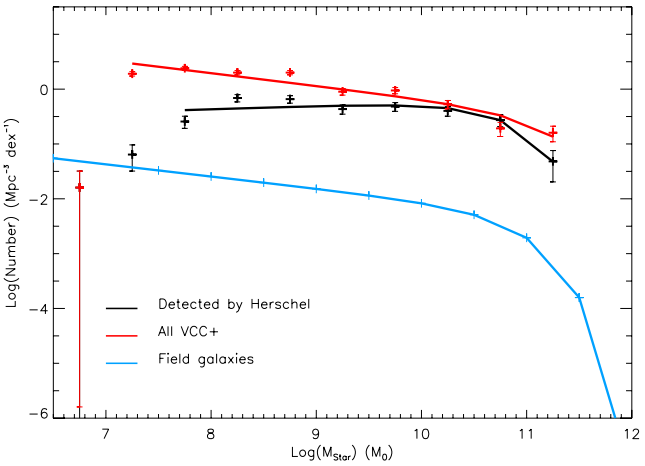

Figure 12. The stellar mass function. The black line and data points are for all 207 galaxies in the *Herschel* sample. The red line and points are for the 691 VCC+ galaxies in our survey area that have a distance of 17–23 Mpc. The blue line shows the field galaxy stellar mass function taken from Panter et al. (2007).

Table 3. Schechter function fitting parameters to the Virgo cluster stellar mass function. For comparisons, we also give the values for the field taken from Panter et al. (2007).

Sample	α	$M^*_{\rm Stars}$ (10^{10} M$_{\odot}$)	ϕ (Mpc^{-3} dex^{-1})	$\rho_{\rm Stars}$ (10^{10} M$_{\odot}$ Mpc^{-3})
Herschel	-0.9 ± 0.1	6.6 ± 1.4	0.6 ± 0.1	1.8
All VCC	-1.2 ± 0.1	19.2 ± 11.7	0.3 ± 0.1	3.3
Field	-1.2	9.5	0.002	0.03

Of course, there are many galaxies detected at optical wavelengths that are not detected by *Herschel*. Using the same prescriptions as described above, we have calculated stellar masses for all 648 VCC galaxies within our survey area with $D = 17$–23 Mpc. We have added to this the 43 new galaxies we detected using the SDSS spectroscopic data (Section 2) giving them the mean cluster distance of 18.7 Mpc – the VCC+ sample (see Table A1). The derived mass function is shown as the red line in Fig. 12. The *Herschel* and VCC+ mass functions coincide at a mass of about 10^{10}–10^{11} M$_{\odot}$ with there being some optically bright early-type galaxies that are not detected by *Herschel* as well as those that are optically faint.

How representative the VCC is of the totality of galaxies in the Virgo cluster has been the subject of much debate in the past. Derived faint-end slopes for the optical luminosity function range from about $\alpha = -1.2$ to -2.0 (Impey, Bothun & Malin 1988; Phillipps et al. 1998; Sabatini et al. 2003). The crucial problem is what remains hidden beneath the rather high surface brightness limit imposed by both the optical data used for the VCC and the SDSS spectroscopic data. Hopefully, the 'Next Generation Virgo Cluster Survey' (NGVCS; Ferrarese et al. 2012) with its low surface brightness sensitivity will soon pass judgement on this issue. In this paper, we will use the stellar mass densities given in Table 3, but note that if all else remains the same then increasing the faint-end slope of the mass function, from -1.2 to -1.7 for example, increases the stellar mass density by a factor of about 2.6. The stellar mass density of the VCC+ sample is about a factor of 1.8 higher than that derived using just the *Herschel* galaxies. This all leads to a cluster stars-to-dust ratio of about 1800 – almost twice the value measured

Table 4. Schechter function fitting parameters to the Virgo cluster H I mass function. For comparisons, we also give the values for the field taken from Davies et al. (2011).

Sample	α	$M^*_{\rm H\,I}$ (10^9 M$_\odot$)	ϕ (Mpc^{-3} dex^{-1})	$\rho_{\rm H\,I}$ (10^9 M$_\odot$ Mpc^{-3})
Herschel	-0.8 ± 0.2	4.1 ± 1.2	0.6 ± 0.2	1.1
All ALFALFA	-1.0 ± 0.2	4.5 ± 1.6	0.6 ± 0.3	1.3
Field	-1.5	5.0	0.009	0.08

for individual galaxies in the *Herschel* sample – there are of course many galaxies with stars, but no detectable dust emission.

For comparison also included in Fig. 12, with fit parameters listed in Table 3, is the field galaxy stellar mass function of Panter et al. (2007). The comparative faint-end slope of the luminosity function in clusters and in the field has been an issue of much debate (Phillipps et al. 1998; Roberts et al. 2004), but is not a problem for us here other than to note that both the VCC+ and field galaxy samples lead to stellar mass functions with the same low-mass slope of $\alpha = -1.2$. The stars-to-dust ratio for the field (Tables 3 and 4) is about 1500, reasonably consistent with that derived above for the cluster (1800). This yet again indicates that these cluster galaxies have not preferably lost dust when compared to galaxies in the field. We again note the lack of galaxies in the cluster with large stellar masses, but as stated above this may just be due to the rarity of bright galaxies and the relatively small volume we are considering.

6 ATOMIC GAS MASS

We have taken our atomic hydrogen data from the ALFALFA data base (Giovanelli et al. 2007). The ALFALFA survey does not completely cover our *Herschel* area missing declinations below 3.°8 and above 16.°2. So, we select data from the survey over this range in declination and over a range of 6.°8 in right ascension to give us the same area on the sky as our *Herschel* survey. We have selected all objects in this area that have a velocity of $400 < v_{\rm Helio} < 2659$ km s^{-1}. The upper bound corresponds to the highest velocity in our *Herschel* detection list of 207 galaxies and the lower bound is set to avoid confusion with Galactic hydrogen and local high-velocity clouds. With this area and velocity range, we hopefully sample about the same volume as the stellar and dust selected samples. Within this volume there are 261 H I detections in the ALFALFA catalogue; 65 of these are not in the VCC and are listed in Table A2. We have used the ALFALFA catalogued values for H I mass and distance and plotted the corresponding H I mass function in Fig. 13 (red line); Schechter function fit parameters are given in Table 4. Using just those galaxies in the *Herschel* sample that have an H I detection we have 133 galaxies; their H I mass function is shown as the black line in Fig. 13, again with Schechter parameters given in Table 4. Finally, in Fig. 13 we show the field galaxy H I mass function (blue line) derived by Davies et al. (2011), and parameters again in Table 4. Note that the H I mass of M31 is just a little higher (6.6×10^9 M$_\odot$) than the values of $M^*_{\rm H\,I}$ we obtain here.

Whereas there is little indication that the dust and stellar masses of low-mass galaxies are greatly affected by the cluster environment, because the cluster and field values of α are effectively the same, this is not true for the atomic hydrogen. The low-mass slope of the field galaxy H I mass function is significantly steeper than that of the cluster. The cluster environment is certainly affecting the H I content of low-mass galaxies. For example, from Table 2 the ratio

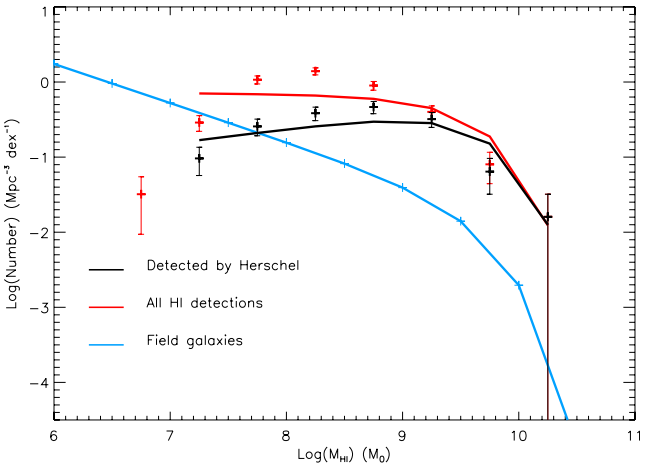

Figure 13. The H I mass function. The red line and points are for the 261 galaxies within our *Herschel* fields that are detected by the ALFALFA survey. The black line and data points are for 133 galaxies in the *Herschel* sample that also have an H I detection. The blue line shows the field galaxy H I mass function taken from Davies et al. (2011).

of dust mass densities between the cluster and the field is ∼90, the same ratio for stars from Table 3 is ∼110, while that for atomic gas is ∼20. If the cluster has an overdensity in baryons by a factor of about 100, as measured by the stars and dust, then the galaxies are depleted in H I by about a factor of 4. This is not a new result as gas depletion in Virgo spirals is discussed extensively in Haynes, Giovanelli & Guido (1984).

What is the origin of this depletion? Broadly, there are two options either the gas has been lost from the galaxies due to their presence in the cluster, most likely by ram pressure, or the gas has been consumed during star formation. We will consider this issue further in Section 8.

If we are trying to understand the differences in the interstellar medium between galaxies in the cluster and the field, which arise because of the environment, one thing to consider is gas(atomic)-to-dust ratios. In the field, this ratio is about ∼400 while in the cluster as a whole it is ∼63 (see Tables 2 and 4).

If we are interested in the total baryon budget in galaxies and also if we want to consider the chemical evolution of galaxies, then we require not just the mass in atomic hydrogen, but the total mass of gas. This includes molecular hydrogen, helium and the mass in the diffuse ionized warm and hot components. These are issues we will discuss in the next section.

7 THE BARYON BUDGET

In the above sections, we have measured and described three important constituents of galaxies, dust, stars and atomic gas, but this is not the totality of the baryons. Although important, the dust and atomic gas components are incomplete because they do not measure all the metals or all of the gas. The dust is only representative of the total amount of metals and the atomic gas of the total gas mass. In this section, we will use some quite sparse data and fits to mass functions to make an estimate of the total mass in metals and gas in our *Herschel* sample galaxies accepting that we have already derived the mass in stars.

As not all of the 207 *Herschel* sample galaxies have an H I mass, for 74 galaxies we have used the dust H I mass correlation to predict an H I mass (Fig. 14, top). The linear least-squares best-fitting line is $\log M_{\rm H\,I} = (0.53 \pm 0.01) \log M_{\rm Dust} + (4.98 \pm 0.04)$.

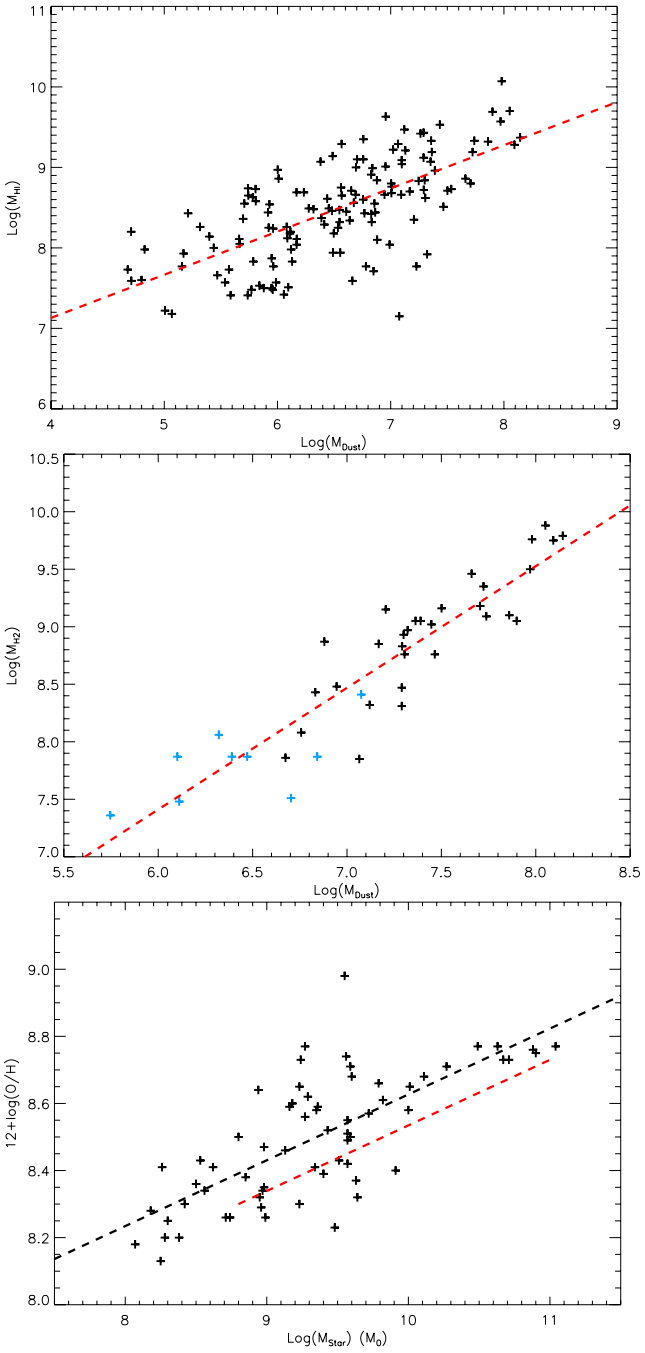

Figure 14. Top: the relationship between calculated ($\beta = 2$) dust mass ($M_{\rm Dust}$) and atomic hydrogen mass ($M_{\rm H\,I}$) – the red dashed line shows the linear least-squares fit to the data. Middle: mass of dust ($M_{\rm Dust}$) against $M_{\rm H_2}$. The black points are for 30 late-type galaxies from Corbelli et al. (2012) and the blue points for 9 early-type galaxies from Young et al. (2011) – the red dashed line shows the linear least-squares fit to the data. Bottom: the stellar mass ($M_{\rm Stars}$) against the oxygen abundance for our sample galaxies is shown as black crosses with the black dashed line showing the linear least-squares fit to the data. The red dashed line shows the relationship for non-Virgo cluster galaxies taken from Hughes et al. 2013 (their fig. 7).

We have obtained from the literature molecular hydrogen gas masses for 39 of our *Herschel* sample galaxies – 30 late types from Corbelli et al. (2012) and 9 early types from Young et al. (2011). In each case, the masses were derived from CO ($J = 1$–0) observations using a constant CO line flux to molecular hydrogen conversion factor of $X_{\rm CO} = 2 \times 10^{20}$ cm^{-2} (K^{-1} km s^{-1})$^{-1}$ (Strong & Mattox 1996). For the 168 galaxies without an H_2 mass, we have used the dust H_2 mass correlation to predicted an H_2 mass (Fig. 14, middle). The linear least-squares best-fitting line is $\log M_{\rm H_2} = (1.06 \pm 0.02) \log M_{\rm Dust} + (1.06 \pm 0.12)$. Note that the relation between molecular gas and dust is approximately linear while that between atomic gas and dust goes approximately as the square root of the dust mass. Only 32 galaxies have both H I and H_2 masses and for these the mean ratio of atomic to molecular hydrogen is 4.2. Recently, for M31 Draine et al. (2013) obtained a value of $M_{\rm H\,I}/M_{\rm H_2} = 19.8$, but the H I was measured over 25 kpc and the H_2 over 12 kpc. Making a simple adjustment for the areas (constant surface density) leads to a value of $M_{\rm H\,I}/M_{\rm H_2} = 4.3$ very close to our mean ratio. We have also corrected the gas mass for the abundance of helium using $M_{\rm H}/M_{\rm He} = 3.0$.

The above provides the correction for cold gas ($T < 10^3$ K), but there is also the hot/warm diffuse ionized gas component of the interstellar medium, which we know much less about. Much of what we know of this ionized component is derived from observations of the Milky Way, and very little is known about its contribution to the baryon content of external galaxies. A comprehensive review of the warm component ($\approx 10^4$ K) is given in Haffner et al. (2009). They discuss Hα observations both of our galaxy and other particularly edge-on galaxies where the diffuse emission can be seen to extend above the mid-plane and above the stars. In summary, Haffner et al. say that the diffuse warm component accounts for about 90 per cent of the ionized hydrogen in galaxies and that this is about one third of the atomic mass. This is confirmed by recent observations of sight-lines to stars in our Galaxy, which again have a mean value of about one third for the ionized to atomic components (Howk & Consiglio 2012).

With regard to the hot component (10^5–10^7 K), there have been a number of observations that infer that this may be a substantial fraction of the total gas mass. One of the main issues is whether this hot gas is actually associated with individual galaxies or if it resides within larger filamentary structures (Tripp, Savage & Jenkins 2000; Gupta et al. 2012). Gupta et al. (2012) have recently claimed that the hot component of the Milky Way has a mass equivalent to that of the stars, in which case it would be the dominant gas phase component. There are two issues with regard to this: the first is that, as said above, this could be material external to the galaxy (particle velocities are of the order of the Galactic escape velocity). Secondly, the values Gupta et al. (2012) use for the solar oxygen abundance and the metallicity of the hot gas are crucial in their calculation. They use a value for the solar oxygen abundance a factor of 1.75 larger than the more recent determination we will use below and although they say that the metallicity of the hot gas is expected to be about 0.2 $z_\odot$ they then go on to use 0.3 $z_\odot$. These two factors combined lead to a factor of 18 increase in the mass derived (they are cubed in the total mass equation). With a factor of 18 decrease in the derived mass, the hot component becomes about one half of the atomic component. Our conclusion is that at the moment it is very difficult to accurately account for the baryons that reside in the combined warm and hot components of galaxies. We have conservatively assigned a mass equivalent to the atomic mass to these two components when we have created our total gas mass function.

For our *Herschel* sample of 207 galaxies, we have used the above correlations and assumptions to obtain total gas masses. For our H I selected sample (ALFALFA), we have used $M_{\rm Gas}^{\rm Tot} \approx 2.5 M_{\rm H\,I}$ derived from the H I mass, the mean ratio of molecular to atomic gas, the abundance of helium and the gas in the warm and hot components to get total gas masses.

We have also obtained from the literature (see Hughes et al. 2013, table 2) oxygen abundance values for 65 galaxies from our *Herschel* sample. Oxygen abundances were obtained using drift scan optical spectroscopy and are based on metallicity calibrations from Kewley & Ellison (2008). We have used the stellar mass–metallicity relation (Fig. 14) to assign a metallicity to those galaxies in the *Herschel* sample that do not have a measured value – a linear least-squares fit gives $12.0 + \log(\mathrm{O/H}) = 0.20 \pm 0.01 \log M_{\mathrm{Stars}} + 6.66 \pm 0.01$. By looking at the residuals after subtracting this linear least-squares fit from the data, we estimate about a 30 per cent error on metallicities calculated in this way. To go from the oxygen abundance to the total metallicity (z), i.e. the total mass of metals in the gas phase, we require the oxygen abundance of the Sun and its metallicity. Asplund & Garcia-Perez (2001) give the solar oxygen abundance as $12.0 + \log(\mathrm{O/H})_{\odot} = 8.69$ and $z_{\odot} = 0.014$ which gives $z = 29.2(\mathrm{O/H})$. The total mass of metals in the gas is then just $zM_{\mathrm{H\,I}}$. Using these numbers we find for our sample galaxies $\langle z \rangle = 0.0093 \pm 0.0003$, about two-thirds of the solar value quoted above, and that the mean fraction of metals in the dust is 0.50 ± 0.02. The fraction of metals in dust has previously been estimated to be 0.5 by Meyer, Jura & Cardelli (1998) and Whittet (1991) and 0.4 by Dwek (1998). Finally, we need to add to this the metals that are in the warm and hot components, which from above we estimate to be $0.2zM_{\mathrm{H\,I}}$ (Gupta et al. 2012) giving $M_{\mathrm{Metals}} = 1.2zM_{\mathrm{H\,I}} + M_{\mathrm{Dust}}$.

Putting all these things together, we can create total mass functions for stars, gas and metals residing in Virgo cluster galaxies. The total stellar mass function is just that given in Fig. 12 and is derived from the optically selected VCC catalogue with additional galaxies selected via their redshift from SDSS (VCC+, 691 galaxies). The total gas mass function is that derived from the H I selected ALFALFA data with each galaxy's gas mass adjusted for molecular hydrogen, helium and gas in the warm and hot components (261 galaxies). The total metal mass function comes from our *Herschel* data (selected via their far-infrared emission), which provides dust masses and to this we add the mass of gas phase metals (207 galaxies).

The mass functions are shown in Fig. 15 and the parameters of the best-fitting Schechter function are given in Table 5 – in each case the lowest mass point is omitted from the fit. The bottom line is that cluster values for the ratios M_{Stars}: M_{Gas}: M_{Metals} as a whole (in galaxies) correspond almost exactly to the canonical values that

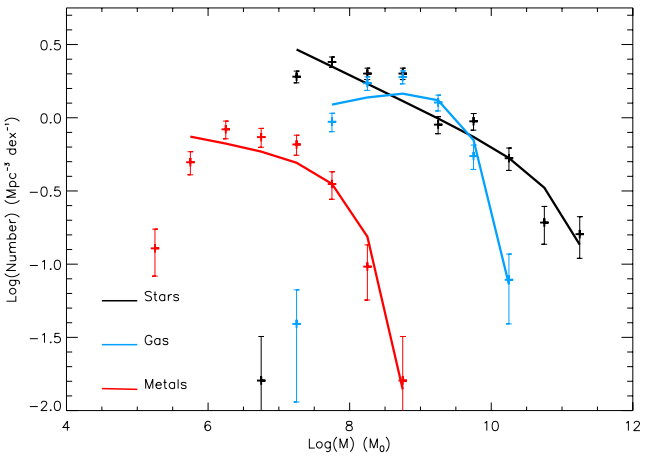

Figure 15. The mass functions for the three baryonic components of galaxies in the Virgo cluster. Black: total stellar mass; blue: total gas mass; red: total mass in metals.

Table 5. Schechter function fitting parameters to the Virgo cluster total mass functions. This is the total mass contained within galaxies. The final column gives the mean cluster densities, which of course vary considerably throughout the cluster. A 1 Mpc box around M87 contains 13.5×10^{10} M$_{\odot}$ Mpc^{-3} of stars due to M87 alone (Davies et al. 2012).

Baryonic component	α	M^* (M$_{\odot}$)	ϕ (Mpc^{-3} dex^{-1})	ρ (M$_{\odot}$ Mpc^{-3})
Total stars	-1.2 ± 0.1	$1.9 \pm 1.2 \times 10^{11}$	0.3 ± 0.1	3.3×10^{10}
Total gas	-0.9 ± 0.1	$5.0 \pm 0.8 \times 10^{9}$	1.8 ± 0.3	4.3×10^{9}
Total metals	-1.1 ± 0.1	$1.7 \pm 0.3 \times 10^{8}$	0.4 ± 0.1	3.3×10^{7}

are normally quoted for the Milky Way, i.e. that the stellar mass is about 10 (8) times the gas mass and that the mass in gas is about 150 (130) times that in metals – values in parentheses are those calculated from Table 5. Although the H I mass function on its own shows that galaxies in the cluster are relatively depleted in atomic hydrogen, the inclusion of helium, molecular, warm and hot gas takes us back to familiar ground.

8 GALAXY SCALING RELATIONS

In this section, we consider four scaling relations for galaxies. First, the relation between gas fraction and metallicity and its interpretation using a chemical evolution model. Secondly, the relation between stellar mass and the current SFR and hence the specific star formation rate (sSFR) of galaxies. Thirdly and fourthly, the baryonic Tully–Fisher relation and the mass–size relation, both of whose origin must presumably lie in the gravitational stability of galaxies. Wherever possible, we will compare our results for the Virgo cluster with those obtained using galaxies that sample the more general galaxy population.

8.1 Chemical evolution

Having the three major baryonic constituents of Virgo cluster galaxies (stars, gas, metals), we can now see if the mass ratios between them are consistent with a chemical evolution model. The simplest model, yet one that provides an insight into how a galaxy evolves chemically, is the closed-box model (Edmunds 1990 and references therein). In its simplest form, this model describes the growth of the fractional mass of metals z in the interstellar medium as a function of the stellar yield p and the gas fraction f. p is the fractional mass of metals per unit mass of gas freshly formed in nucleosynthesis. The above parameters are simply related via $z \leq p \ln(1/f)$. The equality in this equation applies to the closed-box model in which there are no inflows or outflows of gas as the galaxy evolves. More complex models in which various forms of inflow and outflow are described can be found in Edmunds (1990). Edmunds (1990) defines the effective yield as $p_{\mathrm{eff}} = \frac{z}{\ln(1/f)}$, i.e. the derived yield irrespective of whether there are inflows or outflows; he also makes some generalized comments on these cases. For example, models with outflow, but no inflow, or inflow of gas with relatively low metallicity have $p_{\mathrm{eff}} < p$. This is straightforward to understand because unenriched inflow dilutes the interstellar medium while enriched outflow reduces the gas fraction at the same metallicity. Thus, the model can provide an insight into how a galaxy in a specific environment has evolved. Using the data for our 207 *Herschel* galaxies with either measured or predicted values of M_{Star}, M_{Gas} and M_{Metals}, we can compare our data with this simple closed-box model.

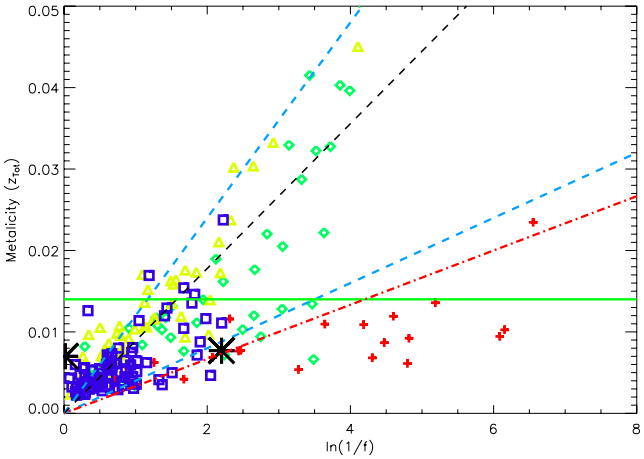

Figure 16. The derived metallicity (metals in both dust and the gas phase) against ln $(1/f)$ for our sample of 207 galaxies, where f is the gas fraction. It is difficult to estimate errors on f given the assumptions we have made (see the text); we expect about 30 per cent errors on the metallicities. Red crosses denote galaxies with type earlier than Sa, green diamonds type Sa/Sb, yellow triangles type Sc and blue squares galaxies later than Sc and dwarfs. The blue dashed lines are for a closed-box model with yields of $p = 0.004$ (bottom) and $p = 0.012$ (top). The solid green line marks the metallicity of the Sun ($z = 0.014$). The red dot–dashed line shows the mass-loss model of Dunne et al. (2011) with a mass-loss of 1.4 times the SFR. The black dashed line shows the best-fitting line to the data. The large black star to the right marks the data for the cluster galaxies as a whole using the total mass densities given in Table 5. The large black star to the left marks the data for the cluster as a whole including X-ray gas.

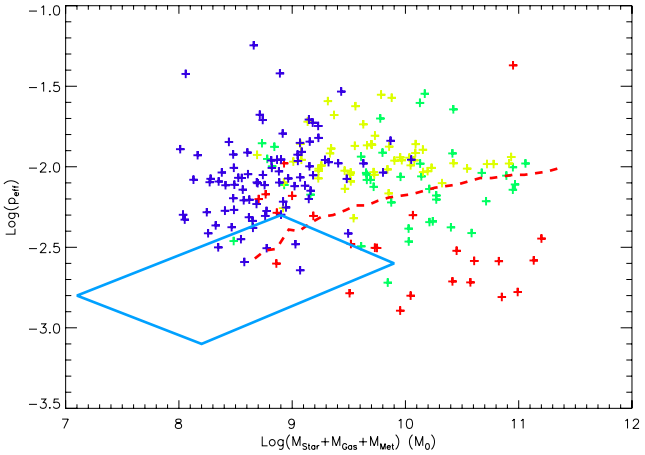

Figure 17. Total baryonic mass against the effective yield ($p_{\rm eff}$). Red is for galaxies with type earlier than Sa, green for type Sa/Sb, yellow for type Sc and blue for galaxies later than Sc and dwarfs. The red dashed line shows the median relation for ∼53 000 SDSS galaxies taken from Tremonti et al. (2004). The blue box represents the area occupied by the Virgo cluster dwarf irregular galaxies studied by Lee et al. (2003).

In Fig. 16, we show the derived value of $z_{\rm Tot} = M_{\rm Metals}/M_{\rm Gas}$ plotted against ln $(1/f)$.[7] Note that the range of metallicities found in individual galaxies is just about the same as that found within different regions of a single galaxy. Within M31, Draine et al. (2013) find a variation of metallicity from about 3 $z_\odot$ at the centre to about 0.3 $z_\odot$ in the outer regions.

If the yield p has a constant value for all galaxies, i.e. purely determined by the physical processes within stars, then we would expect the data shown in Fig. 16 to lie on a straight line; if they evolve as closed boxes, they clearly do not follow this relationship. This result has been known for some time – galaxies do not evolve as closed boxes – however the important issue here is whether cluster galaxies have values of $p_{\rm eff}$ that have been significantly affected by their environment. To decide on this issue, we require a value for the yield p. Vila-Costas & Edmunds (1992) give a value for p in the rather wide range 0.004–0.012. In Fig. 16, we have plotted the two lines (dashed blue) defined by these two values and most of our sample galaxies do lie between these two extremes. The mean value for p obtained from our data is 0.009 ± 0.001 (dashed black line) consistent with the Vila-Costas & Edmunds (1992) values and with the value of 0.0104 obtained by Tremonti et al. (2004) in their recent chemical evolution model of ∼53 000 SDSS galaxies. We conclude that on average Virgo cluster galaxies have a derived value of p consistent with other galaxy samples of predominantly non-cluster galaxies. We find no correlation of $p_{\rm eff}$ with metallicity as might be expected if the fractional mass of metals released back into the interstellar medium is dependent on metallicity, so we assume for the moment that p is a constant and that different positions occupied by galaxies in Fig. 16 reflect changes not in p, but in $p_{\rm eff}$ because of the inflow or outflow of gas. Galaxies are clearly segregated in Fig. 16 when it comes to morphology, though we note that the contribution of hot gas may have been underestimated for the early-type galaxies, in which case the red data points would move to the left.

Based on the assumption that p is a constant, data points below the black line in Fig. 16, and more convincingly below the lower blue line, have values of $p_{\rm eff}$ lower than those might be expected due to stellar processes and could be the result of gas loss. To gain further insight into this issue, we have looked at the relation between $p_{\rm eff}$ and other galaxy properties. In Fig. 17, we plot $p_{\rm eff}$ against the total mass in baryons. Previously, Tremonti et al. (2004) have found, using ∼53 000 SDSS galaxies, that $p_{\rm eff}$ increases with baryonic mass – red dashed line in Fig. 17. Their interpretation of this result is that lower mass galaxies suffer proportionately more from gas loss and so their effective yield is lower, i.e. lower than expected metallicity at a given gas fraction because gas has been lost instead of consumed in stars. Results from the Lee, McCall & Richer (2003) study of Virgo dwarf irregular galaxies qualitatively support this conclusion (Fig. 17). Within our data we find no correlation between galaxy total mass (baryonic) and $p_{\rm eff}$, but we do need to qualify our result. We derive $p_{\rm eff}$ using the metals in both the gas and the dust, not just those in the gas as used by both Tremonti et al. (2004) and Lee et al. (2003). We also use our estimate of the total gas mass while Tremonti et al. resort to inferring the gas mass from the star formation–gas density relation while Lee et al. use the mass of atomic hydrogen. There may also be a selection effect here because we selected galaxies via their emission from their interstellar medium (dust) – Tremonti et al. selected galaxies via emission from stars. As our galaxies have to have an interstellar medium to be detected, maybe the low-mass galaxies in our sample that still have their interstellar medium are young, i.e. there has been insufficient time to have as yet undergone gas loss. Those that have undergone gas loss are just not in our sample.

Emphasized again in Fig. 17 is the trend of increasing values of $p_{\rm eff}$ when going from early to late types. However, investigating this further what we find is a clear relationship between galaxy

[7] Note: $z_{\rm Tot}$ is not the same as the metallicity derived from the oxygen abundance. It includes the mass of metals in the dust and the contribution of helium, H_2, and warm and hot gas to the gas fraction.

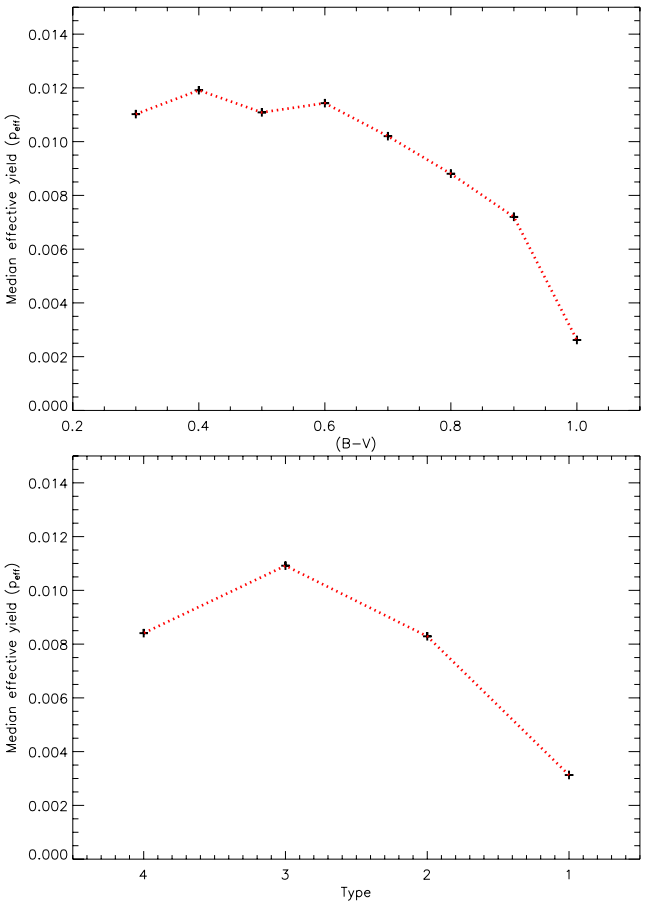

Figure 18. Top: the effective yield against the galaxy ($B - V$) colour. Bottom: the effective yield against galaxy type (1: earlier than Sa, 2: Sa/Sb, 3: Sc and 4: dwarf/BCD/irr).

colour and $p_{\rm eff}$ – red galaxies have lower values of $p_{\rm eff}$ – Fig. 18 (top). Given the lack of a mass–$p_{\rm eff}$ relation, we put this down to an age effect, which fits in with what we said above about a selection effect. The older a galaxy, the more it seems to have been influenced by gas loss processes and $p_{\rm eff}$ has become significantly lower than p. As early-type galaxies tend to be red, we should also see this in a morphology–$p_{\rm eff}$ relation, which we clearly do see in Fig. 18 (bottom). This idea of substantial gas loss by early-type galaxies has been used to explain the origin of metals in the intracluster X-ray gas and will be discussed further in Section 9.

In summary, although the faint end of the H I mass function is flatter than in the field, we do not see any evidence in the chemical evolution that low-mass galaxies have preferentially suffered from gas loss. The simplest explanation is that mass-loss is catastrophic such that we only now see in our sample selected via its interstellar medium those galaxies that are yet to be affected. As the mass-loss seems to be a consequence of being in the cluster (H I mass function), then either these galaxies are young and/or they are recent arrivals. Contrary to this, it is early-type, not necessarily low-mass, galaxies that show the most clear cut signs of gas loss.

If individual galaxies do not behave as closed boxes, does the cluster as a whole? According to White et al. (1993), the baryon fraction in clusters does not change with time – they act as a closed box retaining all information about past star formation and metal production. If true, we can use the stellar, gas and metal mass of the cluster as a whole, i.e. the mass densities given in Table 5, which are derived from the integrals of the mass functions, in a chemical evolution model of the cluster. Note that this is for material in galaxies – we will consider material in the intracluster medium in the next section. These derived mass densities define the total cluster gas mass fraction and metallicity due to material in galaxies. This data point is plotted in Fig. 16 as a large black star and is consistent with a value of $p_{\rm eff}$ that has been significantly affected by galactic gas mass-loss. In this instance, what we mean by gas loss is that it is gas lost by the galaxies, so not available for continued star formation, but it is retained within the cluster.

We have used the outflow model of Dunne et al. (2011) to assess the implications of this gas loss. In their model, we now have $g = \frac{f}{1+R(1-f)}$, where g is the gas mass when there is outflow. $R = \lambda/\alpha$, where λ is the ratio of gas loss rate to the SFR and $\alpha = 0.7$ is the fraction of mass from each generation of star formation tied up in long-lived stars. Our chemical evolution model now becomes $z = \frac{p\,\ln(1/g)}{1+R}$. Using a value of $R = 2$ leads to the red dot–dashed line in Fig. 16 that goes through the data point for the cluster as a whole. A value of $R = 2$ implies that 1.4 times the mass of the stars has been lost from the cluster galaxies. If the cluster evolves as a closed box, retaining this material within the cluster environment, then this lost gas must still reside within the intracluster medium (Section 9).

8.2 The stellar mass–SFR relation

Using galaxies from the Herschel Reference Sample, Hughes et al. (2013) have applied the conversion relations of Iglesias-Paramo et al. (2006) [$\log {\rm SFR_{NUV}}({\rm M_\odot\ yr^{-1}}) = \log L_{\rm NUV}({\rm L_\odot}) - 9.33$] to calculate the SFR of 39 of the 207 galaxies in our *Herschel* sample. Based on the assumption that the shortest far-infrared wavelength, and hence warmest dust, best correlates with the rate at which stars form (Calzetti et al. 2010), we have looked for a correlation between the SFR and our 100 μm data. In Fig. 19, we show that our 100 μm luminosity correlates very well with the calculated SFR derived from the ultraviolet observations. To justify our use of the shortest wavelength data, we have also looked at the correlation between the SFR and our longer wavelength far-infrared data (Fig. 19). The standard deviation of the data about the best-fitting line in a log–log plot is 0.175, 0.183, 0.190, 0.190 and 0.200 for 100, 160, 250, 350 and 500 μm, respectively – the differences are not large, but the

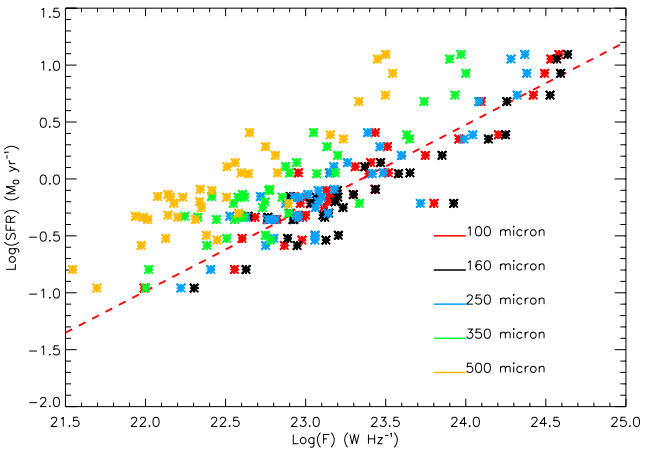

Figure 19. The relationship between far-infrared luminosity in each band and their SFR. The red dashed line shows the fit to the 100 μm data, which has been used to infer SFRs for all 207 galaxies in the *Herschel* sample.

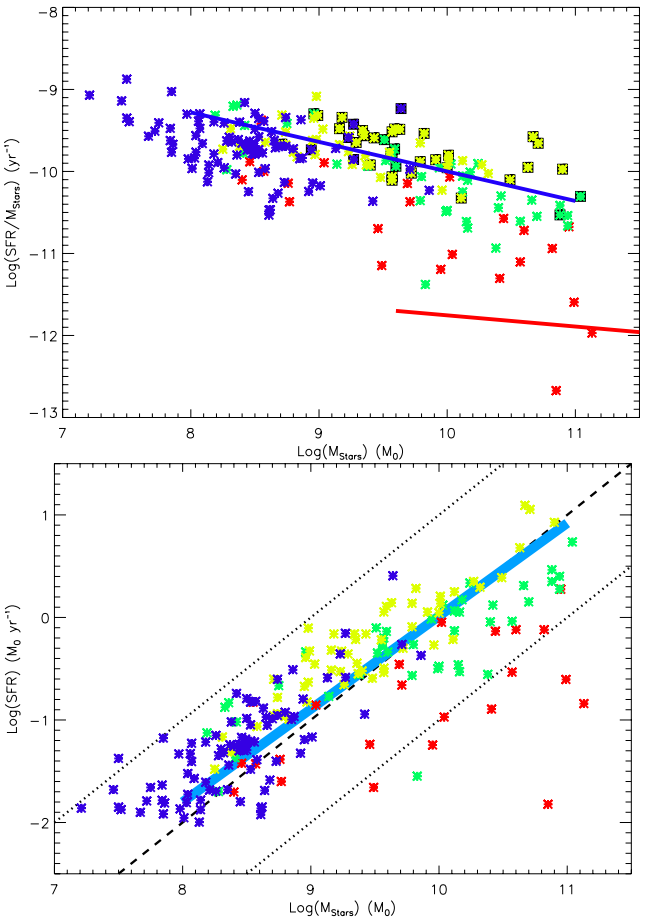

Figure 20. Top: the SFR per unit mass of stars (sSFR) versus the mass of stars. The crosses mark the positions of the 207 galaxies in the *Herschel* sample. Galaxies are distinguished by their morphological type: red denotes galaxies with type earlier than Sa, green type Sa/Sb, yellow type Sc and blue galaxies later than Sc and dwarfs. A black box around the cross marks those galaxies that were used to calibrate the 100 μm SFR relation. The blue line marks the locus of the line of star-forming galaxies and the red line that for passive galaxies (taken from Schiminovich et al. 2007, fig. 7). Bottom: the SFR versus the stellar mass for the 207 galaxies in the *Herschel* sample. The black dashed line indicates an age of 10^{10} yr with the lower and upper dotted lines a factor of 10 older and younger, respectively. The thick blue line indicates the locus of star-forming galaxies (taken from Peng et al. 2010, fig. 1).

100 μm flux density does give the smallest scatter. The relation is $\log \mathrm{SFR}(\mathrm{M}_\odot\ \mathrm{yr}^{-1}) = 0.73 \pm 0.05 \log F_{100}(\mathrm{Jy}) - 17.1 \pm 1.1$.

We have then used this best-fitting relationship to estimate SFRs for all 207 galaxies in our *Herschel* sample. Based on the assumption that our initial optical selection followed by far-infrared detection is not biased against star-forming galaxies, we will use this sample to define the SFR properties of Virgo cluster galaxies and of the cluster as a whole.

In Fig. 20 (top), we have plotted the sSFR, i.e. SFR per unit stellar mass, of our sample against the stellar mass. There is a clear trend for increasing sSFR with decreasing stellar mass. The trend is almost identical to that seen for field galaxies as indicated by the blue line in Fig. 20, which is the locus of the line derived by Schiminovich et al. (2007) using UV derived SFRs for ∼20 000 galaxies (see their fig. 7). In fact, their line ($\log \mathrm{SFR}/M_{\mathrm{Star}} = -0.36 \log M_{\mathrm{Star}} - 6.4$) is almost identical to that obtained by fitting our 39 SFR calibrating galaxies – each one indicated by a black box around each point in Fig. 20 ($\log \mathrm{SFR}/M_{\mathrm{Star}} = -0.30 \pm 0.07 \log M_{\mathrm{Star}} - 6.8 \pm 0.7$). The red line in Fig. 20 (top) is also taken from Schiminovich et al. (2007, fig. 7) and is the locus of what they describe as the non-star-forming sequence. Our conclusion is that our Virgo cluster galaxy sample generally fits the same sSFR–stellar mass relation as is typical for galaxies in the local Universe. We have also distinguished the galaxies, as before, by their morphology. At higher stellar masses we move through S0 and earlier, Sa/Sb then to Sc as we move from lower to higher sSFRs – so the sSFR depends not only on mass, but also on morphology. The very late types/dwarfs have the highest sSFRs.

An alternative way of plotting the same SFR data is shown in Fig. 20 (bottom) – stellar mass against SFR. It is clear that the sSFR defines a time-scale that is straightforwardly illustrated in the bottom plot in Fig. 20. The time-scale is the time to form the current mass of stars at the current SFR – the star formation time-scale. In Fig. 20 (bottom), a time-scale of 10^{10} yr is illustrated by the black dashed line. This line corresponds almost exactly to the locus of star-forming galaxies (light blue line in Fig. 20) obtained using 100 000+ SDSS galaxies by Peng et al. (2010), their fig. 1, and as can be seen is a reasonable fit to our Virgo cluster data. The two dotted lines are for time-scales of 10^{11} and 10^{9} yr for bottom and upper lines, respectively. Galaxies probably undergo vast changes in their SFRs as they age, for example star bursts, but this plot does seem to distinguish galaxies of different types. The naive interpretation is one of younger age when going from red through green to yellow with the dwarf/irregular galaxies predominately young – consistent with what we said when discussing the chemical evolution model.

Using the sum of the SFR of these galaxies and the cluster volume ($62.4\ \mathrm{Mpc}^{-3}$) used before, we estimate a cluster SFR density of $2.0\ \mathrm{M}_\odot\ \mathrm{yr}^{-1}\ \mathrm{Mpc}^{-3}$. This compares with a local SFR density averaged over all environments of $\sim 0.03\ \mathrm{M}_\odot\ \mathrm{yr}^{-1}\ \mathrm{Mpc}^{-3}$ (Robotham & Driver 2011). The cluster has an overdensity in SFR by a factor of ∼66 compared to the local mean value. This is almost a factor of 2 lower than the stellar mass overdensity of ∼110 (Table 3) – a reflection of the increased numbers of quiescent galaxies in the cluster environment.

Multiplying the derived SFR density by the characteristic age of $\sim 10^{10}$ yr gives a stellar mass density of $2.0 \times 10^{10}\ \mathrm{M}_\odot\ \mathrm{Mpc}^{-3}$ compared to that calculated from the integral of the luminosity function of $3.3 \times 10^{10}\ \mathrm{M}_\odot\ \mathrm{Mpc}^{-3}$ (Table 5). So the SFR must have been on average marginally, but not considerably, higher in the past. Given the value of λ calculated in Section 8.1, the chemical evolution model predicts a gas mass-loss rate density of $1.4 \times 2.0 = 2.8\ \mathrm{M}_\odot\ \mathrm{yr}^{-1}\ \mathrm{Mpc}^{-3}$, which amounts to $2.8 \times 10^{10}\ \mathrm{M}_\odot\ \mathrm{Mpc}^{-3}$ of material deposited in the intracluster medium over 10^{10} yr.

Dividing the SFR density by the mass density of stars gives an sSFR for the cluster as a whole of 6.1×10^{-11} (−10.2) yr^{-1} (where the value in parentheses is the log for comparison with Fig. 20). Using the Robotham & Driver (2011) value for the local SFR density and the Panter et al. (2007) value for the local mass density of stars, we get an sSFR for the field of 1.0×10^{-10} (−10.0) yr^{-1}. As already demonstrated in Fig. 20, this comparison of the current sSFR of the Virgo cluster and the local field gives no indication of any dramatic difference between the field and cluster that might be due to environmental effects.

We can also plot the SFR against the gas mass (in this case H I + H_2) of our *Herschel* sample galaxies (Fig. 21). This is effectively the 'global' Schmidt/Kennicutt law (Schmidt 1959; Kennicutt 1998), which usually relates the gas surface density (Σ_{Gas}) to the star formation rate surface density (Σ_{SFR}). Typically and locally within

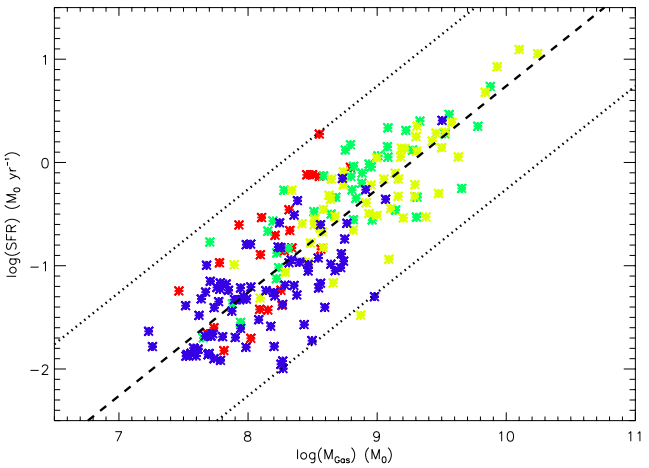

Figure 21. The SFR versus the gas mass for the 207 galaxies in the *Herschel* sample. The black dashed line indicates a gas depletion time-scale of 1.8×10^9 yr with the upper and lower dotted lines a factor of 10 shorter and longer, respectively. Galaxies are distinguished by their morphological type: red denotes galaxies with type earlier than Sa, green type Sa/Sb, yellow type Sc and blue galaxies later than Sc and dwarfs.

galaxies, it is found that $\Sigma_{\rm SFR} = A\Sigma_{\rm Gas}^N$, where $N \approx 1.4$ (Kennicutt 1998). Our 'global' relation, shown in Fig. 21, has a flatter slope than this with an almost linear relation between gas mass and SFR ($N_{\rm Global} = 0.96 \pm 0.04$). This 'global' relation may actually be of more significance than that between the SFR and the mass of stars shown in Fig. 20 (Bigiel et al. 2008). There, because of the large scatter in the data, we just illustrated a line of age 10^{10} yr, but Fig. 21 shows a much better correlation between the data. With a linear relation between gas mass and SFR, the gas sSFR (SFR/$M_{\rm Gas}$) is approximately constant for all galaxies and can be expressed as $\sim 6 \times 10^{-10}$ M$_\odot$ converted into stars each year for each solar mass of gas. The fit to the data also defines the gas depletion time-scale (time to consume the gas at the present SFR) which at 10^9 yr is a factor of 10 shorter than the star formation time-scale defined above. The star formation time-scale describes where a galaxy has been, while the gas depletion time-scale defines where it is going. So, a quantity of interest is the ratio of the gas depletion to the star formation time-scale for galaxies of different morphological types. The median ratio is 0.04, 0.08, 0.38 and 0.51 for our four morphological types, earlier than Sa, Sa/Sb, Sc and later than Sc, respectively. This quantifies a morphological age sequence with those types earlier than Sa at the end of their star-forming lives, while those types later than Sc in their middle age.

8.3 The stellar mass–metallicity relation

In Section 7, we used the mass–metallicity relation to predict metallicities for galaxies in our sample that did not have a measured oxygen abundance. Here we want to briefly discuss the relationship itself. We will not dwell on this point because to some large extent this has already been discussed by us in Hughes et al. (2013). Briefly, there are two major issues with regard to the stellar mass–metallicity relation – its origin and whether it is different in different environments. With regard to its origin, the most common scenario is gas loss due to stellar winds in galaxies of low mass, while larger galaxies retain their gas. This is difficult to sustain within the bounds of our sample as we have already shown that we do not find a global relationship between the effective stellar yield ($p_{\rm eff}$) and baryonic mass – on average our low-mass galaxies do not have lower values of $p_{\rm eff}$ commensurate with gas loss (Fig. 17). As before we suggest that this might be a selection effect, as we have selected galaxies that have as yet not been subject to gas loss.

Having a sample that does not have a lower value of $p_{\rm eff}$ for low-mass galaxies yet still has a mass–metallicity relation leads one to suggest that mass-loss is not the origin of the mass–metallicity relation. Instead, we suggest that what we are seeing is a sequence of age. Low-mass galaxies have large gas fractions (Fig. 16), high sSFRs (Fig. 20, top) and young ages (Fig. 20, bottom).

With regard to the second issue and in agreement with our conclusions in Hughes et al. (2013), we find little evidence for a difference in the stellar mass–metallicity relation with environment. Our data are shown in Fig. 14 (bottom) with a linear least-squares fit indicated by the dashed black line. Note that our sample is larger than that used by Hughes et al. (2013) because we have Virgo galaxies observed by Hughes et al. (2013), which were not in their primary sample. The red dashed line shows the mean relation for non-cluster galaxies taken from Hughes et al. (2013). Although this line apparently sits below our relationship for cluster galaxies, Hughes et al. (2013) use a different prescription for calculating stellar mass [Salpeter rather than the Kroupa initial mass function (IMF)], which we estimate shifts the dashed red line to the left by ≈0.3 dex. Given the scatter in metallicity about the line of ≈0.1 dex, this makes the two lines consistent with each other. We conclude, as in Hughes et al. (2013), that there is no evidence for a higher metallicity at a given stellar mass of cluster compared to field galaxies.

8.4 The baryonic Tully–Fisher relation

One of the most studied, well-defined and used scaling relations for galaxies is the Tully–Fisher relation. The relation was originally used as a means of obtaining distances to galaxies independently of their redshift in order to measure peculiar velocities. It has since been extensively used by numerical simulators of galaxies and large-scale structure to equate something that they measure in their simulation (rotation) to what is observed (luminosity). What is still elusive is the precise physical origin of the Tully–Fisher relation. Given that the Tully–Fisher relation is between velocity and luminosity, the simplest assumption is that luminosity is acting as a proxy for mass (or possibly some combination of mass and size). McGaugh et al. (2000) showed that by using the total baryonic mass (stars plus gas) of a galaxy in place of the luminosity, the scatter in the relation is much reduced – this is known as the baryonic Tully–Fisher relation.

For 100 galaxies from the 207 in the *Herschel* sample, we can obtain from ALFALFA a 21 cm line width (width at 50 per cent of peak flux density – W_{50}) and from NED semi-major (a) and semi-minor (b) axis sizes (measured at the 25th blue magnitude isophote). The axis ratio can be used to obtain the inclination ($\sin i = \sqrt{\frac{1-(b/a)^2}{1-0.15^2}}$; Stark, McGaugh & Swaters 2009) and so correct the measured to the intrinsic velocity width (W_{50}^i). The total baryonic mass ($M_{\rm Tot}$) is just the sum of the mass in stars, gas and metals we used earlier. The relation we obtain is shown in Fig. 22 (black crosses). The gradient of the line (black dashed line) is measured to be 0.29 ± 0.02. This value is reasonably consistent with previously derived values of 0.25 by Stark et al. (2009) and 0.31–0.33 (sample dependent) by Gurovich et al. (2010).

To make a comparison to a data set that samples galaxies over a wide range of environments, not just a cluster, we have selected all 5174 galaxies (Sab or later) from the Lyon extragalactic data base (LEDA) that have an I-band magnitude, a gas mass (atomic

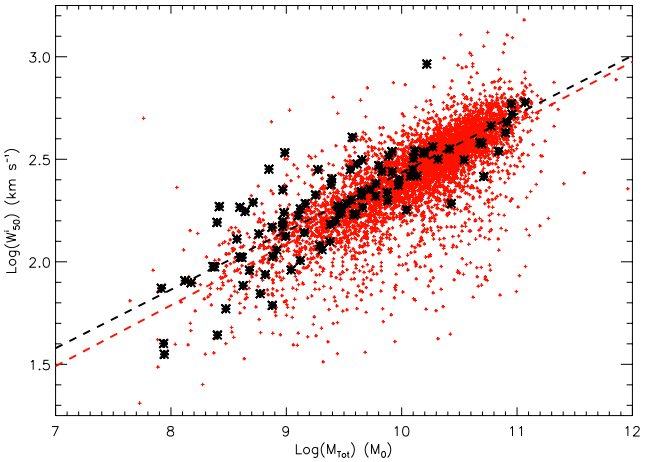

Figure 22. The baryonic Tully–Fisher relation. The black crosses are for 100 Virgo cluster galaxies from the *Herschel* sample. The red dots are for 5174 galaxies taken from the LEDA data base. $M_{\rm Tot}$ is the total baryonic mass for the Virgo galaxies and the stellar plus gas mass for the LEDA galaxies. W^i_{50} is the inclination-corrected velocity width at 50 per cent of the peak flux density for the Virgo galaxies and twice the maximum velocity for the LEDA galaxies.

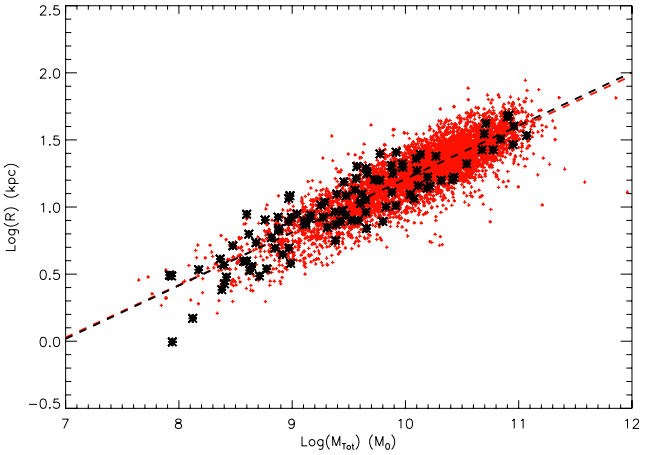

Figure 23. The baryonic mass–size relation. The black crosses are for 100 Virgo galaxies from the *Herschel* sample. The red dots are for 5174 galaxies taken from the LEDA data base. $M_{\rm Tot}$ is the total baryonic mass for the Virgo galaxies and the stellar plus gas mass for the LEDA galaxies. R is the radius measured along the major axis at the 25th $B\mu$ isophote.

hydrogen) and a 'maximum' rotation velocity ($v_{\rm m}$). For each LEDA galaxy, we have then simply obtained a stellar mass using an absolute I-band magnitude for the Sun of $M^I_\odot = 4.08$, a total mass ($M_{\rm Tot}$) by summing the stellar and gas masses and equating W^i_{50} to $2 \times v_{\rm m}$. The data for the LEDA galaxies are shown in Fig. 22 as red dots.

Comparing the cluster and non-cluster data, there appears to be no evidence that the baryonic Tully–Fisher relation is any different for Virgo cluster and non-cluster galaxies. The slope of the line fitted to the LEDA data is 0.297 ± 0.004 (red dashed line) consistent with that for the cluster galaxies and what has been derived before.

8.5 The mass–size relation

Another often quoted scaling relation of galaxies is that between mass and size. Given the data we have for the 100 Virgo cluster galaxies described above, we can also plot the radius (semi-major axis) against the total baryonic mass ($M_{\rm Tot}$) (Fig. 23). The Virgo galaxies again show a good correlation between these two quantities with a measured slope of 0.40 ± 0.02. This compares with a value of 0.32 obtained by Avila-Reese et al. (2008) for a smaller sample of field galaxies.

Again we can use the LEDA data as a comparison sample – red dots in Fig. 23. The measured slope of the relation for the LEDA galaxies is 0.390 ± 0.003 consistent with the Virgo cluster sample. There is no evidence that the cluster environment has altered in any way the global relationship between mass and size – something that might have been expected if, for example, the tenuous outer regions of cluster galaxies were to fall prey to gravitational interactions.

8.6 Comments on the implications of the scaling relations

A typically subscribed explanation of the scaling of the baryonic mass–velocity (T-F) relation (Gurovich et al. 2010, and references therein) starts with an isothermal sphere for which the density is $\rho(r) = \frac{v^2}{4\pi G r^2}$. Then motivated by numerical simulations, regions that collapse into a virialized halo have conventionally a size of r_{200}, which is the size that contains a mean density 200 times that of the critical density. Substituting in this density and size and using $M = \frac{4}{3}\pi\rho_{200} r^3_{200}$ leads to $v \propto M^{1/3}$ – very close to what is observed.

However, there are a number of caveats we should add to this. First, it is not clear how this explanation fits in with the currently favoured galaxy formation model, which relies primarily on the growth of structure through merging of smaller masses and not the collapse of an individual isothermal sphere. Secondly, the argument relies on galaxies all forming from regions of the same initial density; variations in the initial density will produce scatter in the plot and possibly a power-law index not quite equal to 1/3. Thirdly, there are other means (see below) of obtaining this power-law relationship.

With regard to the mass–size relation, the above reasoning leads to $r \propto M^{1/3}$ directly – very close to what is observed – but changes in the initial density will again lead to scatter in the relation. In addition, we also have to accept that a spherical halo of size r_{200} scales linearly to a disc of size $r_{\rm D}$ and that this all happens while each galaxy undergoes substantial merger activity. There are also other ways of obtaining this power-law relationship.

The mass–metallicity and the mass–SFR relations also demonstrate the fundamental role that galaxy mass plays in both the chemical evolution and star formation history of galaxies. Given these four relations, which depend so critically on the mass of a galaxy, one is tempted to surmise that once a galaxy's mass has been laid down almost everything else follows in a well-defined way. As the scaling relations described above seem to apply equally well to cluster and field galaxies, it is clear that internal evolutionary processes dominate over those inflicted by the local environment.

The above is in many ways a restatement of the conclusions of Disney et al. (2008), who showed that out of six primary properties of galaxies five correlated very strongly with one other (mass?). They stated that 'Such a degree of organization appears to be at odds with hierarchical galaxy formation, a central tenet of the cold dark matter model in cosmology.'.

An alternate scenario for individual galaxies, though maybe not such a good explanation of large-scale structure, is that galaxies actually do form from the collapse of approximately isothermal spheres. The collapse of an isothermal sphere, in such a way as to preserve its angular momentum distribution as a function of mass,

leads to a disc with a $1/r$ surface density distribution and a flat rotation curve (a Mestel disc; Mestel 1963). As long as the initial isothermal spheres have the same density, the scaling parameters of such a disc depend only on the initial mass such as $r \propto M^{1/3}$ and $v \propto M^{1/3}$. These relations are the same as those predicted above and are very close to what is observed, but in addition they are much more precisely defined. For example, the Mestel disc parameters (M, r and v) are the same throughout the collapse of the spherical cloud into a disc and there is no issue with mergers (Davies 2012). In addition, there seems to be an age sequence with more massive early types older than the less massive later types – it is difficult to see how this can be accommodated within the current hierarchical picture of galaxy formation.

9 MATERIAL IN THE INTRACLUSTER MEDIUM

As we will see, considering just the galaxies detected in multiwavelength surveys is really just scratching at the surface of the cluster baryon content. In this section, we will review, assess and use data from surveys that have attempted to measure the mass of baryonic material between the galaxies.

Given our expectations of gravitational interactions between the galaxies and with the overall cluster potential, we might expect to find galaxy debris in intergalactic space. It is also not clear how efficient the galaxy formation process is. For example, is star formation confined to the bright easily identifiable galaxies or is there a population of faint stellar systems between the prominent concentrations of stars? And how efficiently has the total cluster gas been taken into the individual stellar systems?

Searches for an intracluster stellar population have previously been made by either looking for the diffuse low surface brightness signal of intergalactic light or by trying to identify individual stars. Beautiful images of the diffuse light in Virgo have been made by Mihos et al. (2005). It seems that this diffuse light is concentrated in extended haloes around the cluster galaxies with the addition of some filamentary structures between them. The first direct detection of individual stars between the galaxies was made by Smith (1981) when he observed a Type Ia supernova in the region between M86 and M84. By comparing source number counts, Ferguson, Tanvir & von Hippel (1998) have inferred the presence of red giant stars in the intergalactic medium. Several groups have used narrow-band imaging to detect intergalactic planetary nebulae (Feldmeier, Giardullo & Jacoby 1998; Arnaboldi et al. 2002, 2003; Feldmeier et al. 2003). In Mihos et al. (2009), the intergalactic light and planetary nebula methods are compared to see whether both are tracing the same stellar structures in the intergalactic medium – the result being 'a rough correspondence on large scales (∼100 kpc)'. Arnaboldi et al. (2003) conclude that about 20 per cent of the light in individual cluster galaxies is produced by intergalactic stars. By simply converting this directly to a mass ($M/L = 1$), we have a mass density of stars outside of galaxies of $\sim 7 \times 10^9\,\mathrm{M_\odot\,Mpc^{-3}}$, a fraction of what is in the galaxies ($3.3 \times 10^{10}\,\mathrm{M_\odot\,Mpc^{-3}}$, Table 5). Hopefully, new surveys like the NGVCS (Ferrarese et al. 2012) will reveal more about the nature of the stars between the brigh galaxies.

Even more so than stars we might expect gas to be removed from galaxies as they move through the cluster environment, for gas is not only affected by gravity, but also by stellar winds and ram pressure stripping by the X-ray gas. Blind surveys for atomic hydrogen in the Virgo cluster have found very little when compared to what is in galaxies. Davies et al. (2004) carried out a blind survey over 32 square degrees of the cluster and found that just 2 per cent of the H I detected was in previously unidentified sources, predominantly in the form of tidal streams. A similar conclusion has been made using the larger area survey of Kent et al. (2007) (see also Kent et al. 2009). We know of no survey that has put limits on the molecular hydrogen and helium mass of material in the intergalactic medium and so adjust for these components in the same way as we have before ($1.7 M_{\mathrm{H\,I}}$). This leads to a mass density of cold/cool gas outside of galaxies of $\sim 9 \times 10^7\,\mathrm{M_\odot\,Mpc^{-3}}$. Again a small fraction of what is in the galaxies ($4.3 \times 10^9\,\mathrm{M_\odot\,Mpc^{-3}}$, Table 5).

Putting the above rough estimates together, the ratio of mass of stars to mass of atomic gas is about 10 times higher in the intergalactic space than in the prominent galaxies. Previously, we have argued that there is good evidence for gas stripping of cluster galaxies and little evidence for the removal of stars, i.e. gas is depleted compared to stars and dust. So, our simple expectation would be just the opposite to what is observed – relatively more gas than stars in the intergalactic medium. Either the intergalactic stars have formed in situ (from stripped or primordial gas) or at sometime in the past gravitational interactions were much more efficient.

However, the relatively cold atomic gas is drawn out via stripping processes but a small fraction of the mass of gas resides between the galaxies. By far the largest contribution to the baryon density in both the intergalactic medium and the cluster as a whole is that due to the hot (X-ray) gas (Bohringer et al. 1994; Urban et al. 2011). It is generally assumed that this gas has been expelled from galaxies by stellar (supernova) winds (Bohringer 2004), hence its high temperature. Observations using *ROSAT* have shown that most of the hot gas is concentrated around the three bright galaxies M87, M86 and M49 with about 83 per cent of the gas mass in the extended halo around M87 and only about 15 per cent in a more diffuse 'cluster' component. The total mass density of hot cluster gas is calculated to be $\sim 10^{12}\,\mathrm{M_\odot\,Mpc^{-3}}$ (we have used 20 per cent of the gravitational mass measured by the X-rays; see Bohringer et al. 1994 for further details). This hot X-ray gas completely dominates the baryon budget with about a factor of 25 more mass in this component than in the stars and cool gas in galaxies and that outside of galaxies combined.

We know of no observations that conclusively show that dust resides in the intergalactic medium of the Virgo cluster,[8] though Cortese et al. (2010a) conclude that dust is being stripped as well as gas from the Virgo cluster galaxy NGC 4438. We will be using the HeViCs, along with other data (21 cm and the reddening of background galaxies), in the future to try and address this issue. In any case, given the dominance of the hot gas we do not expect the metals in intergalactic dust to amount to very much (comparatively). Bohringer et al. (1994) give a metallicity value for the hot gas as $\sim 0.5\,\mathrm{z_\odot}$. This leads to a mass density in metals of $\sim 7 \times 10^9\,\mathrm{M_\odot\,Mpc^{-3}}$, which is about 200 times more than the mass of metals in the galaxies. This is all summarized in Table 6.

Our view of the chemical evolution of the cluster as a whole is now completely changed. In the previous section, we concluded that to be consistent with a simple closed-box chemical evolution model, the cluster galaxies must have lost gas about 1.4 times their stellar mass to the intergalactic medium. In fact, when we do the accounting, we find about a factor of 25 more gaseous material in the intracluster medium than in the stars. This is shown by the position of the left large black star in Fig. 16 (using the total cluster gas fraction and metallicity from Table 6). The closed-box model

[8] Stickel et al. (1998) have previously presented evidence for intergalactic dust emission from the Coma cluster.

Table 6. The total cluster mass within its various components.

Baryonic component	ρ ($M_\odot$ Mpc^{-3})
Total cluster stars	4×10^{10}
Total cluster gas	1×10^{12}
Total cluster metals	7×10^{9}

interpretation of this is that there must have been substantial inflow of enriched gas to get this metallicity at such a high gas fraction. Of course, the closed-box chemical evolution model is not really applicable to the cluster as a whole because the hot gas is not available for continued star formation.

So, how can we interpret the position of the left large black star in Fig. 16 given the White et al. (1993) assertion that baryons are retained within the cluster? If we accept that the galaxies have lost about 1.4 times their stellar mass as outflowing gas, then only about 5 per cent of the intracluster X-ray gas can have its origin from within galaxies and the remaining 95 per cent must have a 'primordial' origin. This is consistent with the numerical models of Matteucci & Gibson (1995), who say that only 1–10 per cent of the intracluster gas can have originated from the galaxies. The immediate conclusion is that within a cluster like Virgo, the galaxy formation process has been very inefficient with only about 5 per cent of the baryonic mass ending up in galaxies. How about the total metallicity of the cluster – can the total mass in metals have been produced by the stars contained within the galaxies? Given the intracluster mass density of metals (7.0×10^9 $M_\odot$ Mpc^{-3}, for an X-ray gas metallicity of 0.5 $z_\odot$; Bohringer et al. 1994) and the predicted mass of outflowing gas ($1.4 \times 3.3 \times 10^{10}$ $M_\odot$ Mpc^{-3}, Table 5), we require a gas outflow from the galaxies with a super solar metallicity of about 13 $z_\odot$. Super solar metallicities like this are possible if the wind consists primarily of supernova ejecta.

To assess if this is a viable explanation of the intracluster metals, we consider a simple model of metal enrichment due to galactic supernova winds. We have used a power-law stellar IMF between 0.1 and 100 $M_\odot$ (Matteucci & Gibson 1995) and the Type II supernova yields given by Arnett (1991) to predict the mass density of metals produced by supernova-driven galactic winds resulting from the observed mass density of stars. We derive the (O/H) ratio and then calculate the total mass in metals assuming solar abundances. For a Salpeter (1955) IMF power-law slope of -2.35, we predict a metal mass density of 3.9×10^8 $M_\odot$ Mpc^{-3} and for a less steep Arimoto & Yoshi (1987) IMF power-law slope of -1.95, 1.4×10^9 $M_\odot$ Mpc^{-3} – this is for 100 per cent efficient supernova mass-loss. Neither of these IMFs can account for the metals found in the intracluster medium, and even with an IMF slope of zero there are insufficient supernova-produced metals to account for the observed metal mass density of 7.0×10^9 $M_\odot$ Mpc^{-3}. We conclude that the 'primordial' intracluster X-ray gas must also have been enriched to some extent by stars other than those found in the galaxies.

We note that the above assumes that the enrichment of the intracluster medium only occurs due to Type II supernovae. This is consistent with the findings of Matteucci & Gibson (1995), who show that later galactic winds due to evolved low-mass stars and Type Ia supernovae generally have insufficient energy to deposit material in the intracluster medium (at most 30 per cent of that deposited by Type II supernovae). If 1.4×10^9 $M_\odot$ Mpc^{-3} is taken as an upper limit on the mass of metals expelled by galaxies, then a lower limit on the metallicity of the 'primordial' gas is $\sim$0.4 $z_\odot$. This is far higher than that expected from models of Population III star gas enrichment which is predicted to be $\sim 10^{-4}$ $z_\odot$ (Trenti & Stiavelli 2009; Kulkarni et al. 2013) and the metallicity of Population II stars, which formed from the Population III enriched gas.

We are thus left with two interesting observations: the gross inefficiency of the galaxy formation process (only 5 per cent of the available baryons end up in galaxies) and the relatively large abundance of metals in this discarded gas. Our result is not controversial as our derived gas-to-total baryon mass fraction of $\approx$0.04 is consistent with models of cluster formation (Planelles et al. 2013) and with observations of other clusters (Vikhlinin et al. 2006). What is difficult to understand is the metallicity of the gas.

If galaxy formation is this inefficient everywhere, then the stellar mass density needs to be multiplied by a factor of $\sim$25 to get the total baryonic mass. Using the field stellar mass density of 3.0×10^8 $M_\odot$ Mpc^{-3} given in Table 3 leads to a predicted baryon density of 8.0×10^9 $M_\odot$ Mpc^{-3} due to this inefficiency. This compares consistently with a baryon density of 6.0×10^9 $M_\odot$ Mpc^{-3} derived from the cosmological model (Komatsu et al. 2011). If this universal inefficiency is true, then most of the baryons involved in the galaxy formation process remain hidden – more evidence for a warm intergalactic medium (Cen & Ostriker 1999) – except in clusters where the large gravitational potential reveals them through their X-ray emission. The origin of the intracluster metals is not clear – they cannot have been synthesized by the stars in galaxies or by a generation of Population III stars. If the origin of the intracluster gas is connected with AGN rather than star formation activity, then the above conclusions will need to be revisited.

10 DARK MATTER AND COSMOLOGICAL IMPLICATIONS

We can obtain an estimate of the total cluster mass in two ways. First, by using the X-ray data to measure both the hot gas mass density and temperature profiles and then assume hydrostatic equilibrium (Briel, Henry & Bohringer 1992). Secondly, by using the line-of-sight velocities of the galaxies and assuming virial equilibrium. Neither of these assumptions, hydrostatic or virial equilibrium, is necessarily true. Clusters including Virgo are observed to have cooling flows within their inner regions and although the hot gas mass distribution is smoother than that of the galaxies it is still clumped on galactic scales (Bohringer et al. 1994). As described in the introduction dynamically, Virgo, along with other clusters, seems to consist of a number of galaxy sub-clusters, clouds, groups and individual galaxies that are currently falling into the cluster and hence have not settled into a virialized mass distribution. Hence, they are not good test particles for measuring the cluster gravitational potential (Binggeli et al. 1987, 1993) – note also the two 'quantized' distances of 17 and 23 Mpc we have used above for cluster members. However, we will use both the X-ray and dynamical data to try and provide some insight into the total cluster mass.

Bohringer et al. (1994) show that the X-ray halo of M87 can be traced out to about 1.5 Mpc ($D_{\rm Virgo}$=17 Mpc) or 5° and that the majority of the gravitating mass, as measured by the X-ray gas, is within this distance. It is clear that the majority of the X-ray emission actually comes from within about 2° of M87 (see fig. 1 in Bohringer et al. 1994), well within the extent of our Herschel data. Based on the assumption of hydrostatic equilibrium, Bohringer et al. (1994) calculate a gravitational mass for the halo around M87 of 1.5–6.0 $\times$ 10^{14} $M_\odot$ – we will take this to be the mean

Table 7. The dynamical properties of the cluster as measured by the various samples and compared with the total mass derived from X-ray observations.

Sample	Number in sample	$\langle v \rangle$ (km s^{-1})	σ_v (km s^{-1})	R_e (Mpc)	$M_{Cluster}$ (10^{14} M$_\odot$)	ρ_{Dyn} (10^{12} M$_\odot$ Mpc^{-3})
Stars (VCC+)	546	1465	590	1.9	4.7	7.5
Gas (ALFALFA)	261	1552	616	1.8	4.7	7.5
Dust (*Herschel*)	146	1475	616	2.2	5.7	9.2
X-ray (Bohringer et al. 1994)	–	–	–	–	4.2	6.7

value of 3.8×10^{14} M$_\odot$. Much smaller haloes around M86 and M49 are calculated to have masses of about 2.0×10^{13} M$_\odot$. This gives a total gravitating mass, as measured by the hot X-ray gas, of $\sim 4.2 \times 10^{14}$ M$_\odot$.

Given the apparent dominance of M87 in the X-ray data, we can regard the cluster galaxies as test particles moving in its gravitational field. In this case, the cluster mass is given by $M_{cluster} = \frac{3\pi}{2G} R_e \sigma_v^2$, where $R_e = \frac{N}{\sum_{i=1}^{N}(|R_i - R_{M87}|)^{-1}}$ is the effective radius of the cluster and $\sigma_v^2 = \frac{\sum_{i=1}^{N}(v_i - v_{M87})^2}{N}$ is the velocity dispersion of the galaxies (Binney & Tremaine 1994). We can use the ALFALFA data we used earlier (261 galaxies with $400 < v_{Helio} < 2659$ km s^{-1}) to make an estimate of the dynamical mass of the cluster. Using these galaxies, we derive a value of $R_e = 1.8$ Mpc and with a measured σ_v of 616 km s^{-1} a cluster mass of $M_{cluster} = 4.7 \times 10^{14}$ M$_\odot$, consistent with the X-ray data. Our mean cluster velocity is measured to be 1552 km s^{-1}, considerably higher than that given in the NED for the cluster (1079 km s^{-1}) and the measured velocity of M87, which is 1258 km s^{-1} (Binggeli et al. 1993). Our exclusion of galaxies with low (<400 km s^{-1}) and negative velocities biases our value compared to other derivations that include them (Binggeli et al. 1993). However, it is the velocity dispersion and not the mean velocity that is important here. Previous measurements of the cluster velocity dispersion give a value of $\sigma = 721$ km s^{-1} (Ferguson & Sandage 1990), a little higher than our value of 616 km s^{-1}. The cluster mass is given in Ferguson & Sandage (1990) as $M_{cluster} = 5.2 \times 10^{14}$ M$_\odot$ when adjusted to a distance of 17 Mpc and as $M_{cluster} = 4.2 \times 10^{14}$ M$_\odot$ when modelled as an NFW halo (McLaughlin 1999). All these values along with that measured by the X-rays are consistent with the value of $M_{cluster} = 4.7 \times 10^{14}$ M$_\odot$ we measure here using the ALFALFA sample galaxies.

As an aside we can also use the stellar and dust samples to measure the dynamical properties of the cluster – 546 galaxies with optical (SDSS) velocities and 146 galaxies in the *Herschel* sample that have H I velocities from ALFALFA. The results are summarized in Table 7 and the distributions of velocities shown in Fig. 24. All three derived cluster masses are consistent with those given above. Given the different spatial distributions of gas-rich and gas-poor galaxies (morphology–density relation), it is surprising that they have almost exactly the same dynamical characteristics, particularly as it is thought that the cluster is being assembled from its infalling gas-rich galaxy population (Boselli & Gavazzi 2006).

The derived effective size of the cluster (R_e) is approximately 2 Mpc (Table 7). Assuming a spherical distribution this gives a cluster volume of 33.5 Mpc^{-3} compared to the value of 62.4 Mpc^{-3} used above. Put another way, we have effectively used a value of $\sim 1.2 R_e$ when calculating the cluster volume.

Galaxies with $400 < v_{Helio} < 2600$ km s^{-1} are used to construct the 'stars' and 'gas' samples shown in Fig. 24 and what is obvious is the bimodal structure obtained by including galaxies from both the sub-clusters and clouds – as described in the introduction. What

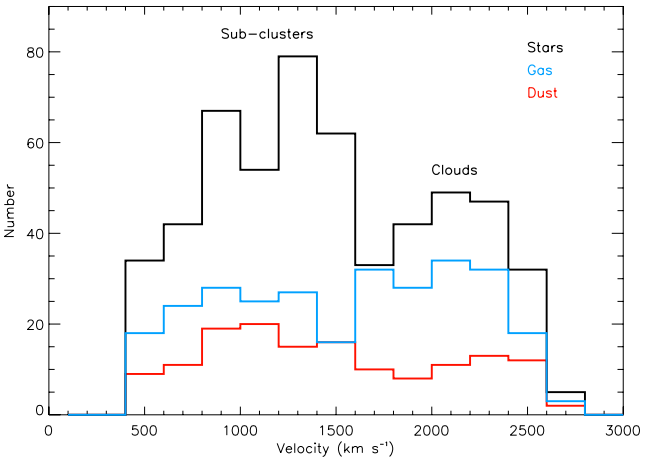

Figure 24. The distribution of galaxy velocities for the three samples. Black denotes 546 galaxies from VCC+, blue 261 galaxies from ALFALFA and red 146 galaxies selected from the *Herschel* sample. The bimodal distribution is due to the cluster sub-structure, which can be split into the two main sub-clusters and two, probably infalling, clouds.

is not so obvious is why this bimodality should also still be present in the *Herschel* data which is restricted to galaxies classified in GOLDMINE as in sub-clusters A and B – either there are some interlopers or the tail of the distribution of sub-cluster velocities extends to velocities that overlap with the clouds.

That the X-rays and the galaxies measure the same gravitational potential can also be checked by comparing the X-ray temperature with that predicted from the velocity dispersion of the galaxies, i.e. $T = \frac{m_p \sigma_v^2}{k_B}$. This gives a value of $T = 3.7 \times 10^7$ K, reasonably close to the measured X-ray temperature of $\sim T = 2.6 \pm 0.3 \times 10^7$ K (Urban et al. 2011).

With a size of $R_e = 1.8$ Mpc and a velocity dispersion of $\sigma_v = 616$ km s^{-1}, the cluster crossing time is of the order of 3×10^9 yr. This is about 1/40th of the Hubble time, 1/3rd of the star formation time-scale, 3 times the gas depletion time and about 10 times the typical rotation period of a galaxy.

The distribution on the sky of the galaxies used to measure the dynamical mass is shown in Fig. 24. Black diamonds denote the 546 galaxies with velocities taken from the VCC+ sample, blue crosses represent the 261 galaxies taken from the H I ALFALFA sample and red crosses show the 146 galaxies with velocities taken from the *Herschel* sample. The large green diamond marks the position of M87, which has been used as the dynamical centre of the cluster. The upper and lower smaller green diamonds mark the positions of M86 and M49, respectively – M87, M86 and M49 are all centres of X-ray emission.

Given a total cluster baryon mass density of about 1.0×10^{12} M$_\odot$ Mpc^{-3}, the cluster is about a factor of ~ 150

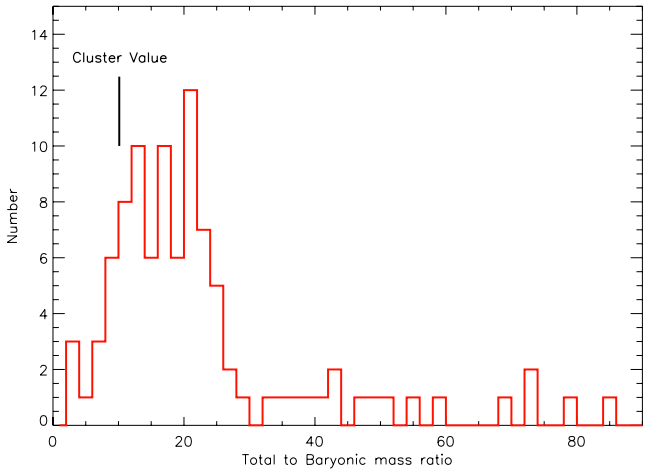

Figure 25. The distribution of dynamical to baryonic mass for 100 Virgo cluster galaxies that have both an H I velocity width and a measured inclination. The black line marks the overall value for the cluster.

more dense in baryons than the cosmologically measured value of $\Omega_b = 0.046$ ($\rho_{Critical} = 1.4 \times 10^{11}\,M_\odot\,Mpc^{-3}$). Given the total dynamical mass density of about $8 \times 10^{12}\,M_\odot\,Mpc^{-3}$, the cluster is about a factor of 200 more dense in all forms of matter than the cosmologically measured value of $\Omega_m = 0.272$ (the above cosmological values are taken from Komatsu et al. 2011). So, the ratio of dynamical (total) to baryonic mass (f_d) for the cluster as a whole is about 8 compared to a value of about 6 for the ratio of total to baryonic matter in the Universe as a whole. Although probably consistent within the impossible-to-estimate errors, higher values of f_d for clusters when compared to the cosmic value have previously been reported by McCarthy, Bower & Balogh (2007). They obtain a mean value for galaxy clusters of $f_d = 8$, the same as we derive here.

We can use our cluster galaxy data to measure this dynamical-to-baryonic mass ratio for individual galaxies. As stated earlier, of the 207 galaxies in our *Herschel* selected sample for which we have measured total baryonic masses there are 100 which have a measured size (R_{ISO}), inclination (i) and an H I velocity width (W_{50}). To estimate individual dynamical masses, we use $M_{dyn} = \frac{R_{ISO} W_{50}^{i\,2}}{G}$, where $R_{ISO} = \sqrt{r_{minor} r_{major}}$ and W_{50}^i is the inclination-corrected velocity width (Cortese et al. 2008). The distribution of dynamical over baryonic mass for these 100 galaxies is shown in Fig. 25; the median value is $f_d \sim 19$ for galaxies. Given that the cluster baryonic mass is dominated by the hot intracluster gas, it is clear that this value of $f_d \sim 19$ for individual galaxies cannot account for the value of $f_d \sim 8$ for the cluster as a whole – confirming the long-held notion that there must also be dark matter in the intergalactic space. There is $\sim 10^{13}\,M_\odot\,Mpc^{-3}$ of dark matter in the cluster as a whole, but only $\sim 10^{12}\,M_\odot\,Mpc^{-3}$ of this can be accounted for by the cluster galaxies.

11 SOME COMMENTS ON THE PROPERTIES OF THE SUB-CLUSTERS

Finally, we will return to something we discussed in the introduction – the structure of the cluster. In this section, we briefly compare the properties of the two sub-clusters, A and B, with the properties of the whole cluster that we have discussed earlier. The data are given in Table 8, and we will comment on each entry in this table. Each parameter has been calculated as described earlier in the text.

Table 8. The derived properties of the Virgo cluster compared to those of sub-clusters A and B as defined by galaxies detected by *Herschel*.

	Virgo	Sub-cluster A	Sub-cluster B
Number	207	147	60
Morphology			
Per cent type 1	12	12	12
Per cent type 2	20	20	22
Per cent type 3	27	26	28
Per cent type 4	41	42	38
M_{Stars} ($M_\odot$)	2.1×10^{12}	1.8×10^{12}	2.6×10^{11}
M_{Gas} ($M_\odot$)	2.7×10^{11}	2.2×10^{11}	5.0×10^{10}
M_{Metals} ($M_\odot$)	2.1×10^{9}	1.7×10^{9}	3.8×10^{8}
M_{X-rays} ($M_\odot$)	8.4×10^{13}	7.6×10^{13}	4.0×10^{12}
M_{Stars}/M_{Gas}	7.8	8.4	5.2
M_{Gas}/M_{Metals}	129	128	132
p_{eff}	0.009	0.009	0.009
$\langle v \rangle$ (km s^{-1})	1475	1515	1409
σ_v (km s^{-1})	616	609	629
R_e (Mpc)	2.2	2.0	1.4
V (Mpc^3)	62.4	57.8	18.7
$M_{Dynamical}$ ($M_\odot$)	5.7×10^{14}	5.2×10^{14}	3.8×10^{14}
$M_{Dynamical}/M_{Baryon}$	8	7	88
SFR density ($M_\odot$ yr^{-1} Mpc^{-3})	2.0	1.8	1.2

Binggeli et al. (1987) using optical data describe sub-cluster A as being rich in early-type galaxies compared to sub-cluster B. In our *Herschel* sample, we find no difference in the morphological mix of the two sub-clusters (Table 8). This is perhaps not surprising because early-type galaxies will always be underrepresented in a sample selected by emission from the interstellar medium.

We have obtained the masses of stars, gas and metals given in Table 8 by just summing the masses of all the 207 galaxies in the *Herschel* sample. This gives values for the cluster as a whole that are different by factors of 1.02, 1.59 and 1.7 for stars, gas and dust, respectively, from those given in Table 5, which were obtained by integrating the mass functions (then using the density given in Table 5 multiplied by the volume of 62.4 Mpc^{-3} to give the mass). We have adjusted the values given in Table 8 using the above factors so that they are consistent with Table 5. It is clear that sub-cluster A contains by far the majority of the mass, for example 85 per cent of the stellar mass is in sub-cluster A.

The ratios of mass of stars (M_{Stars}) to mass of gas (M_{Gas}) and mass of gas (M_{Gas}) to mass of metals (M_{Metals}) are both pretty consistent for both sub-clusters, though sub-cluster B is more gas rich compared to sub-cluster A. The mean effective yield (p_{eff}), as described in Section 8.1, is the same for each sub-cluster indicating that their chemical evolutionary history is very much the same.

Both sub-clusters have about the same calculated mean velocity ($\langle v \rangle$), but note the discussion in Section 10 above about not including galaxies with velocities less than 400 km s^{-1}. The similarity of mean velocities makes it difficult to distinguish sub-cluster membership without independent distance information (Gavazzi et al. 1999). Velocity dispersions (σ_v) are very similar for both the cluster and both the sub-clusters. Sub-cluster B is characterized by a smaller effective radius (R_e). The volumes (V) have been calculated, assuming spherical distributions and sizes of $1.2R_e$ – Section 10.

Not only does sub-cluster A dominate the baryonic mass, it also dominates the dynamically measured mass ($M_{Dynamical}$) with 91 per cent of the total mass. Given the factor of 10 difference in stellar mass between sub-clusters A and B, it is surprising that sub-cluster B has a dynamical mass only a factor of ~0.7 smaller

than A. This is reflected in the dynamical-to-baryonic mass ratio ($M_{\rm Dynamical}/M_{\rm Baryon}$, where $M_{\rm Baryon}$ is the total mass in stars, gas, metals and X-ray gas), which is a factor of more than 10 larger than that for the cluster as a whole and sub-cluster A. The sub-cluster B dynamical mass is also discrepant when compared with the gravitating mass measured by the X-rays, which at $2 \times 10^{13}\,{\rm M}_{\odot}$ is more than a factor of 10 less than that measured by the dynamics. Using the gravitating mass calculated from the X-rays leads to a value of $M_{\rm Dynamical}/M_{\rm Baryon} = 5$. However, Bohringer et al. (1994) note that the X-ray emission of M49, at the centre of sub-cluster B, is much more centrally condensed than that of the spatial distribution of galaxies in the sub-cluster and that the relation between gravitational mass and gas mass may be more like that of an isolated galaxy (Nulsen, Stewart & Fabian 1984). In that case, we may have underestimated $M_{\rm X-ray}$ by as much as a factor of 100, making the problem even worse. It is difficult to know what is going on here, whether there is a problem, and if there is whether it is with $M_{\rm Dynamical}$ or $M_{\rm X-ray}$.

Finally, the SFR density has been calculated using the sum of the SFRs in each sub-cluster and the volume (V). These rate densities do not vary greatly between the sub-clusters. Note that the SFR densities for the sub-clusters are less than that of Virgo because their combined volume is greater than that of Virgo.

12 CONCLUSIONS

(i) Faint galaxy number counts both on and off the cluster field indicate that the optical selection of galaxies does not miss a population of previously undetected cluster far-infrared sources.

(ii) Cluster luminosity functions are generally flatter at the faint end than those derived for field galaxies – the cluster lacks faint far-infrared sources.

(iii) The cluster dust mass function has a similar shape to that of field galaxies so the differences in the luminosity functions must be due to temperature – more low dust mass star-forming galaxies in the field.

(iv) The cluster is overdense in dust by about a factor of 100 compared to the field (Table 2).

(v) Individual galaxies have a range in global dust temperatures similar to that found in different regions of a typical galaxy like M31 (15–25 K).

(vi) Individual galaxies have the same $T-\beta$ relation as that found in different regions of a typical galaxy like M31.

(vii) We have used SDSS data to optically identify 43 new cluster members to add to those already listed in the VCC.

(viii) The cluster stellar mass function has a similar shape to that of the field and the cluster. The cluster is overdense in stars by about a factor of 100 compared to the field (Table 3).

(ix) We used ALFALFA data to identify 65 new H I detections that are not in the VCC.

(x) The cluster atomic gas mass function is far less steep than that of the field. The cluster is overdense in atomic gas by only about a factor of 16 compared to the field – consistent with the loss of gas, but not stars and dust in the cluster environment (Table 4).

(xi) The mean metallicity of cluster galaxies is about $0.7\,{\rm z}_{\odot}$, and 50 per cent of the metals are in the gas phase with the rest residing in the dust.

(xii) We adjust the atomic gas masses for the contributions of He, H_2, and warm and hot gas to get the total gas mass. We use the observed values of (O/H) to measure the mass of metals in the gas phase.

(xiii) The mass density of stars in galaxies is 8 times that of the gas and the gas mass density is 130 times that of the metals (Table 5).

(xiv) We consider a chemical evolution model using the total mass of baryons in stars, gas and metals. We find no relation between the effective yield and mass, but as there is a mass–metallicity relation we suggest that this relation may be more the consequence of age differences rather than a consequence of preferential mass-loss by low-mass galaxies.

(xv) The chemical evolution model predicts that the cluster galaxies have lost about 1.4 times their stellar mass to the intergalactic medium.

(xvi) The effective yield depends on galaxy colour and morphological type – earlier type galaxies, not particularly ones of lower mass, seem to have lost more of their mass to the intergalactic medium.

(xvii) Cluster galaxies appear to follow the same sSFR versus stellar mass relation as those in the field – lower mass galaxies have higher sSFRs.

(xviii) Lower mass late-type galaxies have shorter star formation time-scales and longer gas depletion time-scales than more massive earlier types – they are middle aged compared to the old age of the early types.

(xix) The gas sSFR is approximately constant for all galaxies.

(xx) Cluster galaxies follow the same baryonic Tully–Fisher relation as field galaxies.

(xxi) Cluster galaxies follow the same mass–size relation as field galaxies.

(xxii) Given how well many galaxy properties scale with galaxy mass, it is not easy to see how this can be accommodated within a hierarchical picture of galaxy formation. In addition, it seems that the least massive galaxies are the youngest.

(xxiii) The presence of the intergalactic X-ray gas, at first sight, just indicates that the galaxy formation process is very inefficient; however, within any scenario it is difficult to account for the origin of the gas' metallicity and hence the origin of the gas itself. The X-ray gas is not consistent with gas loss from the cluster galaxies or with the production of metals within galactic stars.

(xxiv) The cluster is about 150 times more dense in baryons than the cosmologically measured value of $\Omega_{\rm b}$.

(xxv) The cluster is about 200 times more dense in all forms of matter than the cosmologically measured value of $\Omega_{\rm m}$.

(xxvi) Dark matter in the individual galaxies cannot account for the total mass density of the cluster.

(xxvii) The two sub-clusters A and B, as detected by *Herschel*, are similar in their morphological mix and in most other respects. The main exception is mass, with the baryonic mass of sub-cluster A being about an order of magnitude larger than sub-cluster B. It is not clear whether either the dynamic or the X-ray data can provide a good estimate of the gravitational mass of sub-cluster B.

ACKNOWLEDGEMENTS

The *Herschel* spacecraft was designed, built, tested and launched under a contract to ESA managed by the Herschel/Planck Project team by an industrial consortium under the overall responsibility of the prime contractor Thales Alenia Space (Cannes), including Astrium (Friedrichshafen) responsible for the payload module and for system testing at spacecraft level, Thales Alenia Space (Turin) responsible for the service module and Astrium (Toulouse) responsible for the telescope, with in excess of a hundred sub-contractors.

PACS has been developed by a consortium of institutes led by MPE (Germany), including UVIE (Austria); KU Leuven, CSL, IMEC (Belgium); CEA, LAM (France); MPIA (Germany); INAF-IFSI/OAA/OAP/OAT, LENS, SISSA (Italy); IAC (Spain). This development has been supported by the funding agencies BMVIT (Austria), ESA-PRODEX (Belgium), CEA/CNES (France), DLR (Germany), ASI/INAF (Italy) and CICYT/MCYT (Spain).

SPIRE has been developed by a consortium of institutes led by Cardiff University (UK) and including Univ. Lethbridge (Canada); NAOC (China); CEA, LAM (France); IFSI, Univ. Padua (Italy); IAC (Spain); Stockholm Observatory (Sweden); Imperial College London, RAL, UCL-MSSL, UKATC, Univ. Sussex (UK); and Caltech, JPL, NHSC, Univ. Colorado (USA). This development has been supported by national funding agencies: CSA (Canada); NAOC (China); CEA, CNES, CNRS (France); ASI (Italy); MCINN (Spain); SNSB (Sweden); STFC (UK); and NASA (USA).

This research has made use of the NASA/IPAC Extragalactic Database (NED) which is operated by the Jet Propulsion Laboratory, California Institute of Technology, under contract with the National Aeronautics and Space Administration.

Funding for the SDSS and SDSS-II has been provided by the Alfred P. Sloan Foundation, the Participating Institutions, the National Science Foundation, the US Department of Energy, the National Aeronautics and Space Administration, the Japanese Monbukagakusho, the Max Planck Society and the Higher Education Funding Council for England. The SDSS website is http://www.sdss.org/. The SDSS is managed by the Astrophysical Research Consortium for the Participating Institutions. The Participating Institutions are the American Museum of Natural History, Astrophysical Institute Potsdam, University of Basel, University of Cambridge, Case Western Reserve University, University of Chicago, Drexel University, Fermilab, the Institute for Advanced Study, the Japan Participation Group, Johns Hopkins University, the Joint Institute for Nuclear Astrophysics, the Kavli Institute for Particle Astrophysics and Cosmology, the Korean Scientist Group, the Chinese Academy of Sciences (LAMOST), Los Alamos National Laboratory, the Max-Planck-Institute for Astronomy (MPIA), the Max-Planck-Institute for Astrophysics (MPA), New Mexico State University, Ohio State University, University of Pittsburgh, University of Portsmouth, Princeton University, the United States Naval Observatory and the University of Washington.

This publication makes use of data products from the Two Micron All Sky Survey, which is a joint project of the University of Massachusetts and the Infrared Processing and Analysis Center/California Institute of Technology, funded by the National Aeronautics and Space Administration and the National Science Foundation.

We acknowledge the usage of the HyperLeda data base (http://leda.univ-lyon1.fr).

IDL is a postdoctoral researcher of the FWO-Vlaanderen (Belgium).

REFERENCES

Aannestad P., 1975, ApJ, 200, 30
Abazajian K. et al., 2009, ApJS, 182, 543
Arimoto N., Yoshi Y., 1987, A&A, 173, 23
Arnaboldi M. et al., 2002, AJ, 123, 760
Arnaboldi M. et al., 2003, AJ, 125, 514
Arnett D., 1991, in Lambert D., ed., ASP Conf. Ser. Vol. 20, Frontiers of Stellar Evolution. Astron. Soc. Pac., San Francisco, p. 389
Asplund M., Garcia Perez A., 2001, A&A, 372, 601
Auld R. et al., 2013, MNRAS, 428, 1880
Avila-Reese V., Zavala J., Firmani C., Hernandez-Toledo H., 2008, AJ, 136, 1340
Baes M. et al., 2014, A&A, submitted
Baes M. et al., 2010, A&A, 518, 53
Bell E., McIntosh Daniel H., Katz N., Weinberg M., 2003, ApJS, 149, 289
Bendo G. et al., 2003, AJ, 125, 2361
Bendo G. et al., 2012, MNRAS, 419, 1833
Bianchi S., 2013, A&A, 552, 89
Bicay M., Giovanelli R., 1987, ApJ, 321, 645
Bigiel F., Leroy A., Walter F., Brinks E., de Blok W., Madore B., Thornley M., 2008, AJ, 136, 2846
Binggeli B., Sandage A., Tammann G. A., 1985, AJ, 90, 1681
Binggeli B., Tammann G., Sandage A., 1987, AJ, 94, 251
Binggeli B., Popescu C., Tammann G., 1993, A&AS, 98, 275
Binney J., Tremaine S., 1994, Galactic Dynamics. Princeton Univ. Press, Princeton, NJ, p. 610
Bohringer H., 2004, in Duc P. J., Braine J., Brinks E., eds, Proc. IAU Symp. 217, Recycling Intergalactic and Interstellar Matter. Astron. Soc. Pac., San Francisco, p. 92
Bohringer H., Briel U. G., Schwarz R. A., Voges W., Hartner G., Trümper J., 1994, Nature, 368, 828
Boselli A., Gavazzi G., 2006, PASP, 118, 517
Boselli A. et al., 2010, A&A, 518, 61
Boselli A. et al., 2011, A&A, 528, 107
Boselli A. et al., 2012, A&A, 540, 54
Briel U., Henry J., Bohringer H., 1992, A&A, 259, L31
Calzetti D. et al., 2010, ApJ, 714, 1256
Cen R., Ostriker J., 1999, ApJ, 514, 1
Chung A., van Gorkom J., Kenney J., Crowl H., Vollmer B., 2009, AJ, 139, 1741
Clemens M. et al., 2010, A&A, 518, 50
Clemens M. et al., 2013, MNRAS, 433, 695
Clements D. et al., 2010, A&A, 518, L8
Corbelli E. et al., 2012, A&A, 542, 32
Cortese L. et al., 2008, MNRAS, 383, 1519
Cortese L., Bendo G., Isaak K., Davies J., Kent B., 2010a, MNRAS, 403, 26
Cortese L. et al., 2010b, A&A, 518, 49
Cortese L. et al., 2012, A&A, 540, 52
Cote P. et al., 2004, ApJS, 153, 223
Coupeaud A. et al., 2011, A&A, 535, A124
Dale D. et al., 2012, ApJ, 745, 95
Davies J., 2012, preprint (arXiv:1204.4649)
Davies J. et al., 2004, MNRAS, 349, 922
Davies J. et al., 2010, A&A, 518, 48
Davies J. et al., 2011, MNRAS, 415, 1883
Davies J. et al., 2012, MNRAS, 419, 3505
De Looze I. et al., 2010, A&A, 518, 54
Desert F. et al., 2008, A&A, 481, 411
di Serego Alighieri S. et al., 2013, A&A, 552, 8
Disney M., Romano J., Garcia-Appado D., West A., Dalcanton J., Cortese L., 2008, Nature, 455, 1082
Draine B. et al., 2013, preprint (arXiv:1306.2304v1)
Dressler A., 1980, ApJ, 236, 351
Dunne L. et al., 2011, MNRAS, 417, 1510
Dwek E., 1998, ApJ, 501, 643
Eales S. et al., 2010, PASP, 122, 499
Edmunds M., 1990, MNRAS, 246, 678
Feldmeier J., Giardullo R., Jacoby G., 1998, ApJ, 503, 109
Feldmeier J., Ciardullo R., Jacoby G. H., Durrell P. R., 2003, ApJS, 145, 65
Ferguson H., Sandage A., 1990, AJ, 100, 1
Ferguson H., Tanvir N., von Hippel T., 1998, Nature, 391, 461
Ferrarese L. et al., 2012, ApJS, 200, 4
Galametz M. et al., 2012, MNRAS, 425, 763
Gavazzi G., Boselli A., Scodeggio M., Pierini D., Belsole E., 1999, MNRAS, 304, 595

Gavazzi G., Boselli A., Donati A., Franzetti P., Scodeggio M., 2003, A&A, 400, 451
Giovanelli R. et al., 2005, AJ, 130, 2598
Giovanelli R. et al., 2007, AJ, 133, 2569
Gordon K. D. et al., 2010, A&A, 518, 89
Grossi M. et al., 2010, A&A, 518, 52
Gupta A., Mathur S., Krongold Y., Velton A., Veeraraghavan A., Rasker R., 2012, ApJ, 756, 8
Gurovich S., Freeman K., Jerjen H., Stavely-Smith L., Puerari I., 2010, 140, 676
Haffner L. et al., 2009, Rev. Mod. Phys., 81, 969
Haynes M., Giovanelli R., Guido C., 1984, ARA&A, 22, 445
Howk C., Consiglio M., 2012, ApJ, 759, 97
Hughes T., Cortese L., Boselli A., Gavazzi G., Davies J. I., 2013, A&A, 550, 115
Iglesias-Paramo J. et al., 2006, ApJ, 164, 381
Impey C., Bothun G., Malin D., 1988, ApJ, 330, 891
Kennicutt R., 1998, ApJ, 498, 541
Kent B. et al., 2007, ApJ, 665, 15
Kent B. et al., 2009, ApJ, 691, 1595
Kewley L., Ellison S., 2008, ApJ, 681, 1183
Komatsu E. et al., 2011, ApJS, 192, 18
Kulkarni G., Rollinde E., Hennawi J., Vangioni E., 2013, ApJ, 772, 93
Lagache G., Abergel A., Boulanger F., Puget J., 1998, A&A, 333, 709
Lee H., McCall M., Richer M., 2003, AJ, 2975, 2997
Li A., 2004, in Block D. L., Puerari I., Freeman K. C., Groess R., Block E. K., eds, Proc. ASSL, Vol. 319, Penetrating Bars Through Masks of Cosmic Dust: The Hubble Tuning Fork Strikes a New Note. Kluwer, Dordrecht, p. 535
Lis D. C., Serabyn E., Keene J., Dowell C. D., Benford D. J., Phillips T. G., Hunter T. R., Wang N., 1998, ApJ, 509, 299
Magnelli B. et al., 2013, A&A, 553, 132
Magrini L. et al., 2012, MNRAS, 427, 1075
Matteucci F., Gibson B., 1995, A&A, 304, 11
McCarthy I., Bower R., Balogh M., 2007, MNRAS, 377, 1457
McGaugh S., Schombert J., Bothun G., de Blok W., 2000, ApJ, 533, 99
McLaughlin D., 1999, ApJ, 512, L9
Mei S. et al., 2007, ApJ, 655, 144
Mei S. et al., 2010, BAAS, 42, 514
Meny C., Gromov V., Boudet N., Bernard J.-Ph., Paradis D., Nayral C., 2007, A&A, 468, 171
Mestel L., 1963, MNRAS, 126, 553
Meyer D., Jura M., Cardelli J., 1998, ApJ, 493, 222
Mihos C., Harding P., Feldmeier J., Morrison H., 2005, ApJ, 631, 41
Mihos C., Janowiecki S., Feldmeier J., Harding J., Morrison H., 2009, ApJ, 698, 1879
Negrello M. et al., 2013, MNRAS, 429, 1309
Neugebauer G. et al., 1984, ApJ, 278, L1
Nulsen P., Stewart G., Fabian A., 1984, MNRAS, 208, 185
Panter B., Jimenez R., Heavens A., Charlot S., 2007, MNRAS, 378, 1550
Pappalardo C. et al., 2012, A&A, 545, 75
Paradis D., Bernard J., Meny C., 2009, A&A, 506, 745
Peng Y. et al., 2010, ApJ, 721, 193
Phillipps S., Driver S., Couch W., Smith R., 1998, ApJ, 498, 119
Planck Collaboration, 2011, A&A, 536, A24
Planelles S., Borgani S., Dolag K., Ettori S., Fabjan D., Murante G., Tornatore L., 2013, MNRAS, 431, 1487
Remy-Ruyer A. et al., 2013, A&A, 557, 95
Roberts S. et al., 2004, MNRAS, 352, 478
Robotham A., Driver S., 2011, MNRAS, 413, 257
Sabatini S., Davies J., Scaramella R., Smith R., Baes M., Linder S. M., Roberts S., Testa V., 2003, MNRAS, 341, 981
Salpeter E., 1955, ApJ, 121, 161
Sanders D., Mazzarella J., Kim D., Surace J., Soifer B., 2003, AJ, 126, 1607
Schiminovich D. et al., 2007, ApJS, 173, 315
Schmidt M., 1959, ApJ, 129, 243
Seki J., Yamamota T., 1980, Ap&SS, 72, 79
Shapley H., Ames A., 1926, Harvard Circ., 294
Shetty R., Kauffmann J., Schnee S., Goodman A., 2009, ApJ, 696, 676
Skibba R. et al., 2011, ApJ, 738, 123
Skrutskie M. et al., 2006, AJ, 131, 1163
Smith H., 1981, AJ, 86, 998
Smith M. et al., 2010, A&A, 518, 51
Smith M. et al., 2012a, ApJ, 748, 123
Smith M. et al., 2012b, ApJ, 756, 40
Stark D., McGaugh S., Swaters R., 2009, AJ, 138, 392
Stepnik B. et al., 2003, A&A, 398, 551
Stickel M., Lemke D., Mattila K., Haikala L. K., Haas M., 1998, A&A, 329, 55
Strauss M. et al., 2002, AJ, 93, 498
Strong A., Mattox J., 1996, A&A, 308, 421
Taylor R., 2010, PhD thesis, Cardiff University, UK
Tremonti C. et al., 2004, ApJ, 613, 913
Trenti M., Stiavelli M., 2009, ApJ, 694, 879
Tripp T., Savage B., Jenkins E., 2000, ApJ, 534, 1
Urban O., Werner N., Simionescu A., Allen S., Bohringer H., 2011, MNRAS, 414, 210
Vikhlinin A., Kravtsov A., Forman W., Jones C., Markevitch M., Murray S. S., Van Speybroeck L., 2006, ApJ, 640, 691
Vila-Costas M., Edmunds M., 1992, MNRAS, 259, 121
Warren S. et al., 2007, MNRAS, 375, 213
White S., Navarro J., Evard A., Frenk C., 1993, Nature, 366, 429
Whittet D., 1991, Dust in the Galactic Environment. IoP Publishing, Bristol
Young L. et al., 2011, MNRAS, 414, 940

APPENDIX A

Table A1. Virgo Cluster Catalogue Additional (VCCA) galaxies detected using SDSS data.

Name	RA (2000) (^{h} ^{m} ^{s})	Dec. (2000) ($^{\circ}$ $'$ $''$)	v_{Helio} (km s^{-1})	g (mag)
VCCA1	12 11 40.3	12 58 24.6	2220	18.3
VCCA2	12 11 45.9	13 17 07.9	2466	18.2
VCCA3	12 11 53.9	13 48 30.3	2016	17.3
VCCA4	12 11 59.5	05 55 02.7	759	17.2
VCCA5	12 12 40.7	06 50 27.8	2286	17.7
VCCA6	12 14 23.5	06 45 51.0	2154	16.2
VCCA7	12 14 28.2	05 54 31.3	1944	16.8
VCCA8	12 14 44.6	12 47 22.7	2292	17.9
VCCA9	12 14 44.9	06 09 16.2	2064	17.6
VCCA10	12 15 17.1	06 23 35.4	2136	17.6
VCCA11	12 16 10.1	15 07 25.3	570	17.5
VCCA12	12 16 20.6	14 46 26.1	525	17.9
VCCA13	12 17 44.8	06 04 57.6	2478	17.1
VCCA14	12 17 46.6	05 22 36.2	2013	18.0
VCCA15	12 18 04.9	07 44 45.0	2166	18.3
VCCA16	12 18 20.6	04 51 13.6	2100	16.7
VCCA17	12 18 28.3	06 04 33.9	2250	18.3
VCCA18	12 19 27.8	04 34 42.6	1584	16.1
VCCA19	12 19 28.5	06 16 22.6	1530	17.8
VCCA20	12 19 49.2	05 11 06.1	1968	16.2
VCCA21	12 19 53.7	06 01 56.4	1992	18.1
VCCA22	12 20 30.9	06 38 23.8	1497	18.2
VCCA23	12 20 35.0	05 48 27.3	2190	17.1
VCCA24	12 20 56.3	05 11 20.5	2355	18.1
VCCA25	12 21 22.5	05 56 51.7	1785	17.0
VCCA26	12 22 04.7	07 44 22.0	1344	17.2
VCCA27	12 22 43.6	05 27 23.0	2310	18.2
VCCA28	12 22 59.6	08 01 51.4	648	17.0
VCCA29	12 23 03.2	05 47 09.5	2064	18.2
VCCA30	12 25 04.2	15 42 40.7	1398	17.0
VCCA31	12 25 31.5	11 09 30.1	906	17.3

Table A1 – *continued*

Name	RA (2000) (^{h} ^{m} ^{s})	Dec. (2000) ($^{\circ}$ $'$ $''$)	v_{Helio} (km s^{-1})	g (mag)
VCCA32	12 25 51.2	07 47 14.9	660	18.3
VCCA33	12 26 24.9	10 34 54.8	1026	18.7
VCCA34	12 26 47.9	07 40 17.6	618	15.7
VCCA35	12 26 49.1	09 34 27.9	867	14.1
VCCA36	12 29 14.6	07 52 39.1	1530	15.8
VCCA37	12 29 51.2	14 03 59.3	1518	19.8
VCCA38	12 30 02.6	09 24 11.8	924	17.4
VCCA39	12 31 52.9	12 15 59.1	969	18.0
VCCA40	12 33 40.3	12 44 13.6	1146	18.5
VCCA41	12 33 44.7	10 59 39.8	1161	17.4
VCCA42	12 33 56.4	07 42 25.8	828	18.0
VCCA43	12 37 34.3	08 28 55.2	1527	18.3

Table A2. VCCA galaxies detected at 21 cm using ALFALFA data.

Name	RA (2000) (^{h} ^{m} ^{s})	Dec. (2000) ($^{\circ}$ $'$ $''$)	v_{Helio} (km s^{-1})	W_{50} (km s^{-1})	Line flux (Jy km s^{-1})
VCCA44	12 10 38.2	13 01 22.0	2394	34	0.56
VCCA45	12 11 59.8	05 54 53.0	752	33	0.39
VCCA46	12 12 01.6	10 24 08.0	1637	69	0.87
VCCA47	12 12 59.2	07 18 03.0	2162	71	0.67
VCCA48	12 13 10.1	13 34 32.0	2100	94	0.69
VCCA49	12 13 41.8	12 53 52.0	2235	53	1.30
VCCA50	12 13 49.8	05 21 01.0	1690	49	0.99
VCCA51	12 14 11.7	12 47 21.0	613	90	0.68
VCCA52	12 14 13.7	08 54 22.0	1933	95	2.07
VCCA53	12 14 26.7	05 55 01.0	1921	110	0.96
VCCA54	12 14 41.4	12 46 43.0	2279	44	0.39
VCCA55	12 14 55.8	09 40 03.0	1693	31	0.34
VCCA56	12 15 28.2	10 31 14.0	1990	59	0.83
VCCA57	12 16 12.8	08 21 59.0	862	21	0.35
VCCA58	12 16 27.5	06 03 00.0	2029	79	1.94
VCCA59	12 16 34.3	10 12 35.0	2072	38	0.91
VCCA60	12 17 27.1	12 55 49.0	2056	66	0.62
VCCA61	12 17 27.4	07 19 46.0	2202	137	1.68
VCCA62	12 17 33.8	14 23 47.0	2111	64	0.60
VCCA63	12 17 49.1	15 04 52.0	2200	40	0.54
VCCA64	12 17 55.5	14 44 45.0	1990	128	2.30
VCCA65	12 17 59.7	08 09 50.0	2000	98	0.87
VCCA66	12 18 05.1	14 45 16.0	1763	47	0.48
VCCA67	12 18 11.1	04 38 13.0	2073	37	0.39
VCCA68	12 18 47.7	04 48 12.0	1822	103	0.80
VCCA69	12 19 16.8	06 15 21.0	1983	51	0.84

Table A2 – *continued*

Name	RA (2000) (^{h} ^{m} ^{s})	Dec. (2000) ($^{\circ}$ $'$ $''$)	v_{Helio} (km s^{-1})	W_{50} (km s^{-1})	Line flux (Jy km s^{-1})
VCCA70	12 19 18.8	06 24 10.0	1969	44	1.60
VCCA71	12 19 20.4	12 57 10.0	2164	57	0.77
VCCA72	12 19 30.5	06 00 45.0	1622	52	0.60
VCCA73	12 19 42.5	05 35 15.0	2381	56	0.58
VCCA74	12 19 57.8	05 26 01.0	2474	62	0.88
VCCA75	12 20 37.5	14 36 08.0	587	29	0.31
VCCA76	12 20 40.5	05 06 09.0	1691	74	0.71
VCCA77	12 20 41.5	05 54 30.0	978	48	0.48
VCCA78	12 20 49.7	05 58 60.0	1772	46	0.32
VCCA79	12 21 12.7	10 37 19.0	2606	37	0.51
VCCA80	12 22 33.7	04 40 28.0	2214	103	0.89
VCCA81	12 23 17.8	05 36 19.0	1787	178	0.90
VCCA82	12 23 57.5	07 26 57.0	1229	55	0.66
VCCA83	12 24 04.7	08 17 35.0	1370	56	1.13
VCCA84	12 24 48.6	07 54 23.0	797	20	0.31
VCCA85	12 24 51.0	04 03 17.0	1771	34	0.37
VCCA86	12 25 32.4	11 09 13.0	900	48	0.36
VCCA87	12 26 01.8	08 10 18.0	1304	33	1.14
VCCA88	12 26 19.4	12 53 30.0	2246	135	2.25
VCCA89	12 27 13.7	07 38 18.0	1179	44	1.28
VCCA90	12 29 30.4	08 47 12.0	539	36	0.35
VCCA91	12 29 42.8	09 41 54.0	524	116	1.24
VCCA92	12 29 58.3	08 26 04.0	609	53	0.49
VCCA93	12 30 19.4	09 35 18.0	603	252	2.84
VCCA94	12 30 25.8	09 28 01.0	488	62	2.74
VCCA95	12 30 44.4	05 50 06.0	2346	96	0.82
VCCA96	12 30 44.4	05 52 11.0	2332	52	0.57
VCCA97	12 31 19.0	09 27 49.0	607	56	0.76
VCCA98	12 31 26.7	09 18 52.0	480	53	0.97
VCCA99	12 32 08.2	05 50 11.0	1838	39	0.59
VCCA100	12 32 23.8	05 54 37.0	1830	50	0.66
VCCA101	12 32 36.5	06 00 58.0	1799	112	0.90
VCCA102	12 33 08.4	05 51 47.0	1917	32	0.92
VCCA103	12 33 15.5	05 02 19.0	1825	29	0.76
VCCA104	12 33 34.5	06 02 30.0	1872	104	1.05
VCCA105	12 33 36.9	06 26 43.0	1804	103	2.19
VCCA106	12 34 02.6	05 57 49.0	648	21	0.43
VCCA107	12 34 45.3	12 46 49.0	785	145	0.95
VCCA108	12 35 06.9	02 30 51.0	1692	101	1.82
VCCA109	12 35 23.1	05 02 32.0	1805	37	0.46

This paper has been typeset from a TEX/LATEX file prepared by the author.